



Dry wear and corrosive wear behavior of laser-cladded $\text{Co}_{19.6}\text{Cr}_{19.6}\text{Fe}_{19.6}\text{Ni}_{19.6}(\text{B}_{13.72}\text{Si}_{5.88})_{19.6}\text{Y}_2$ and $\text{Fe}_{43.6}\text{Ni}_{17.4}\text{Cr}_9\text{Co}_6\text{B}_{17.5}\text{Si}_{1.5}\text{Nb}_5$ coatings

Zeng Junshan ^{a,b}, Chen Liang ^{a,b}, Lan Yuankuo ^{a,b}, Cheng Yuhao ^{a,b}, Xu Luqian ^{a,b}, Jiang Haoli ^c, Ding Zhibing ^{a,b}, Zhang Jianfeng ^c, Liu Bin ^d, Guo Wenmin ^{a,b,d,*}

^a College of Mechanical and Energy Engineering, Shaoyang University, Shaoyang 422000, China

^b Key Laboratory of Hunan Province for Efficient Power System and Intelligent Manufacturing, Shaoyang University, Shaoyang 422000, China

^c College of Mechanics and Materials, Hohai University, Nanjing 211100, China

^d State Key Laboratory of Powder Metallurgy, Central South University, Changsha 410083, China

ARTICLE INFO

Keywords:

High-entropy alloy

Laser cladding

Corrosive wear behavior

ABSTRACT

Corrosive wear is a key factor affecting the safe operation of offshore engineering equipment. In this study, $\text{Co}_{19.6}\text{Cr}_{19.6}\text{Fe}_{19.6}\text{Ni}_{19.6}(\text{B}_{13.72}\text{Si}_{5.88})_{19.6}\text{Y}_2$ and $\text{Fe}_{43.6}\text{Ni}_{17.4}\text{Cr}_9\text{Co}_6\text{B}_{17.5}\text{Si}_{1.5}\text{Nb}_5$ coatings were prepared on the surface of 304 stainless steel using laser cladding technology. Dry wear and corrosive wear behavior of both coatings and 304 stainless steel were comparatively studied under different loads. The results show that both coatings are mainly composed of FCC solid solution, boride, and Laves phases. The average microhardness of $\text{Co}_{19.6}\text{Cr}_{19.6}\text{Fe}_{19.6}\text{Ni}_{19.6}(\text{B}_{13.72}\text{Si}_{5.88})_{19.6}\text{Y}_2$ and $\text{Fe}_{43.6}\text{Ni}_{17.4}\text{Cr}_9\text{Co}_6\text{B}_{17.5}\text{Si}_{1.5}\text{Nb}_5$ coatings are 578.6 HV_{0.2} and 632.5 HV_{0.2}, respectively. The dry wear resistance of $\text{Fe}_{43.6}\text{Ni}_{17.4}\text{Cr}_9\text{Co}_6\text{B}_{17.5}\text{Si}_{1.5}\text{Nb}_5$ coating is approximately 3 times that of 304 stainless steel under all friction load conditions. It can be found that the $\text{Fe}_{43.6}\text{Ni}_{17.4}\text{Cr}_9\text{Co}_6\text{B}_{17.5}\text{Si}_{1.5}\text{Nb}_5$ coating with high hardness is less sensitive to friction load changes during dry wear process. In 3.5 wt% NaCl solution, the corrosive wear resistance of CoCrFeNiBSiY coating under friction loads of 30 N and 50 N is 2.68 times and 2.83 times that of 304 stainless steel, respectively. The excellent corrosive wear resistance performance of the CoCrFeNiBSiY coating is mainly attributed to its superior corrosion resistance and repassivation ability. During the corrosive wear process, a dense passivation film is formed on the surface of both coatings, which significantly reduces their friction coefficient and volume loss rate.

1. Introduction

Marine engineering equipment such as drilling platforms, wind power platforms, and underwater robots have long been exposed to complex service conditions where corrosion and wear coexist, resulting in serious surface damage to key components and even catastrophic failures [1]. With the increasing demand for resource exploration in extreme environments, the moving parts of marine engineering equipment have put forward high requirements for the comprehensive performance of engineering materials, such as high strength and toughness under wide temperature ranges, superior corrosion and wear resistance, excellent low-temperature impact resistance, etc. [2].

Stainless steel is a commonly used structural material in marine environments [3]. However, 304 stainless steel is prone to martensitic

phase transformation under the coupling effect of corrosion and wear, which in turn causes galvanic corrosion, resulting in a decrease in its corrosive wear resistance [4]. Studies have shown that the corrosive wear resistance of 2205 stainless steel is also degraded due to the σ phase transformation [3]. The development of advanced materials and surface coating technologies is one of the effective methods to solve the corrosion-wear coupling failure of materials in extreme environments. Li et al. [5] prepared a Ni coating on the surface of 304 stainless steel using a combination of sandblasting and electrodeposition. The coating exhibits excellent corrosion resistance. However, the experimental process of sandblasting-electrodeposition-sandblasting is complicated. Oxide ceramic coatings have excellent corrosion resistance due to their chemical inertness. Mohan et al. [6] prepared a nanostructured $\text{ZrO}_2\text{-TiO}_2$ coating on the surface of 304 stainless steel by the sol-gel dip

* Corresponding author at: College of Mechanical and Energy Engineering, Shaoyang University, Shaoyang 422000, China.

E-mail address: wenminguo@hotmail.com (G. Wenmin).

coating process. The corrosion resistance of stainless steel is significantly increased by 88.21 % with the additional coating. However, the coating exhibits low hardness and poor wear resistance.

Due to the unique high-entropy effect, severe lattice distortion, diffusion retardation, and “cocktail” effect, high-entropy alloys (HEA) exhibit high hardness, excellent wear resistance, superior corrosion resistance, etc. [7–10]. It is considered to be one of the promising materials for preparing protective coatings for marine engineering equipment. Laser cladding technology has been widely used in the field of repair and remanufacturing of engineering equipment. Laser cladding coatings have demonstrated a series of comprehensive advantages, such as low dilution rate, refined microstructure, and superior metallurgical bonding with the substrate [11–13]. Liu et al. [14] reported that the corrosion current density of laser cladded CoCrNi coating in acidic rainwater is 2 orders of magnitude lower than that of 304 stainless steel. Ma et al. [15] reported that laser cladded CoCrNi-WC composite coatings exhibit high hardness and excellent wear resistance. However, the galvanic corrosion generated between various strengthening phases and the FCC matrix leads to the deterioration of the corrosion resistance of the coating. Literature research shows that [16] refining the reinforcing phase is beneficial to improving the corrosion and wear resistance of the coating. In addition, doping with elements such as Mo, Nb or Ta can also improve the corrosion resistance of high-entropy alloys with FCC structures [17]. Fu et al. [18] reported that the CoCr2FeNiMo0.3 coating exhibits excellent performance under the synergistic effects of corrosion and wear in 3.5 wt% NaCl acidic solution. High-entropy amorphous nanocrystalline coatings also have excellent corrosion and wear resistance properties [19,20]. Shang et al. [21] found that the existence of Cr and the amorphous phase also promotes the passivation phenomenon and improves the corrosion resistance of the Fe₄₄Cr₃₀Mo₂₀B₃C₃ amorphous nanocrystalline coating.

Literature research shows that high-entropy composite coatings have excellent corrosion and wear resistance. However, the key factors affecting corrosive wear performance are still unclear. Generally, the corrosive wear performance of materials can be comprehensively evaluated through four aspects: pure corrosion, pure wear, corrosion-accelerated wear, and wear-accelerated corrosion [18,22,23]. Fu et al. [18] reported that corrosion-induced wear and wear-induced corrosion are the main factors affecting the corrosive wear behavior of CoCrFe-NiMo coatings in simulated seawater. The effects of pure corrosion cannot be ignored either. Wen et al. [24] found that the NiCrCoFeMoNb coating did not undergo obvious corrosion during corrosive wear. Research by Hua [25] et al. found that the wear rate of TiZrNbTaMo HEA in PBS solution was lower than that under dry wear conditions, indicating that there is no corrosion accelerated wear effect. In addition, the PBS solution also acts as a lubrication, thereby reducing the friction coefficient and inhibiting the wear process. Cao et al. [26] reported that the main factors affecting corrosive wear performance may be related to external factors such as applied load and corrosive environment.

In order to further clarify the corrosive wear mechanism of high-entropy alloy coatings, CoCrFeNiBSiY high-entropy alloy powder was designed and prepared through argon atomization technology. Commercial FeNiCrCoBSiNb amorphous nanocrystalline powder was selected for comparison. CoCrFeNiBSiY and FeNiCrCoBSiNb coatings were prepared on the surface of 304 stainless steel using laser cladding technology. The microstructure and mechanical properties of both coatings were characterized. The dry wear and corrosive wear behavior of both coatings and 304 stainless steel were investigated. The mechanisms of dry wear and corrosive wear were discussed.

2. Experimental procedures

2.1. Preparation and characterization of gas-atomized powders

High-purity metal elements (99.99 %) were selected as raw materials. According to the nominal composition shown in Table 1, alloy

Table 1

Nominal chemical composition of CoCrFeNiBSiY and FeNiCrCoBSiNb powders (at.%).

	Co	Cr	Fe	Ni	B	Si	Y	Nb
CoCrFeNiBSiY	19.6	19.6	19.6	19.6	13.72	5.88	2	–
FeNiCrCoBSiNb	6	9	43.6	17.4	17.5	1.5	–	5

ingots with uniform composition were obtained through multiple arc melting processes (ZH001, Peshing New Metal (Changzhou) Co., Ltd., Changzhou, China.). Then, CoCrFeNiBSiY and FeNiCrCoBSiNb powders were prepared using argon atomization technology(HERMIGA 100–30 V2ICC, Peshing New Metal (Changzhou) Co., Ltd., Changzhou, China.). The atomized gas pressure is 2.0–6.0 MPa. The powders were sieved using airflow classification technology.

The phase identification of spherical powders was carried out using X-ray diffractometer (AL-2700B, Dandong Aolong Radiative Instrument Group Co., Ltd., Dandong, China). The target material is copper, the working voltage is 40 kV, the working current is 30 mA, and the scanning speed is 5°/min. To characterize the cross-sectional microstructure of the powders, phenolic resin was mixed with the powders. Metallographic samples of both powders were prepared with a metallographic sample mounting machine (ZXQ-100, Shanghai Zhongyan Instrument Manufacturing Co., Ltd., Shanghai, China). The samples were ground with sandpaper and then polished with diamond pastes (Wuyi Hengyu Instrument Co., Ltd., Jinhua, China) with a particle size of 1.3 μm and 1 μm in sequence. The surface morphology and cross-sectional morphology of both powders were characterized using scanning electron microscopy equipped with a backscattered electron detector (Phenom ProX, Thermo Fisher Scientific Inc., Eindhoven, The Netherlands). The working voltage is 15 kV, and the beam current is 390 pA. The particle size distribution of both powders was analyzed using a laser particle size analyzer (Mastersizer 3000, Malvern Panalytical Ltd., UK). The nitrogen and oxygen content of the powder was detected using an oxygen, nitrogen, and hydrogen analyzer (TCH-600, LECO Corporation, USA).

2.2. Preparation of laser-cladded coatings

304 stainless steel with a size of 100 mm × 50 mm × 12 mm was selected as the substrate. Its chemical composition is shown in Table 2. The surface of the 304 stainless steel was cleaned using laser cleaning technology (Clean Star-H100, Changsha worldstar laser technology Co., Ltd., Changsha, China). The process parameters of laser cleaning are shown in Table 3. The coating was prepared on the surface of 304 stainless steel using a laser cladding system under a high-purity argon atmosphere (HLC30, Changsha worldstar laser technology Co., Ltd., Changsha, China). The laser cladding system is equipped with four independent coaxial powder feeding devices. The powder feeding rate of each powder feeding device can be adjusted individually. The process parameters for preparing laser cladded coatings are shown in Table 4.

2.3. Microstructure characterization and microhardness measurement

The phase identification of the laser cladded coatings was carried out using an X-ray diffractometer (AL-2700B, Dandong Aolong Radiative Instrument Group Co., Ltd., Dandong, China). Metallographic samples of laser cladded coatings were prepared using a metallographic sample mounting machine with phenolic resin. The samples were ground with sandpaper and then polished. The cross-sectional micromorphology of the laser cladded coatings was characterized using field emission scanning electron microscopy equipped with a backscattered electron detector (Tescan Mira4, TESCAN GROUP, Czech Republic). The working voltage is 20 keV, and the beam current is 1 nA. The microhardness of the laser cladded coatings was tested using a Vickers hardness tester (DHV-1000Z, Shanghai Shangcui Testing Machine Co., Ltd.,

Table 2

Chemical composition of 304 stainless steel (wt%).

C	Mn	P	S	Si	Cr	Ni	N	Fe
0.08	2	0.035	0.015	0.75	18–20	8–10.5	0.1	Balance

Table 3

Process parameters of laser cleaning.

Laser power (W)	laser frequency (kHz)	Laser pulse width (ns)	Laser spot width (mm)	Laser cleaning speed (mm/s)	Number of reciprocating cleaning cycles
80	200	100	50	1–5	10

Shanghai, China). The applied load is 1.96 N and the load duration is 15 s. Select a position every 0.1 mm in the cross-section of the coating along the thickness direction of the cladding layer for hardness testing. The microhardness value at each location is the average of three measurements.

2.4. Electrochemical measurements

Electrochemical tests including potentiodynamic polarization (PDP) and electrochemical impedance spectroscopy (EIS) were carried out using an electrochemical station (CHI600E, Shanghai Chenhua Instrument Co., Ltd., Shanghai, China.) with a three-electrode cell system in 3.5 wt% NaCl solution at room temperature ($\sim 25^\circ\text{C}$). Before testing, the samples were welded with Cu wire and then cold mounted in epoxy resin, leaving only an area of 1 cm^2 of the coating exposed. The coating surface is polished according to the above procedure. A platinum sheet and a saturated calomel electrode (SCE) were used as counter electrode and reference, respectively. The open circuit potential (OCP) of prepared specimen was measured for about 30 min to achieve a relatively stable surface. The PDP curves are carried out with potential range from $-1.0\text{ V}_{\text{SCE}}$ to $1.5\text{ V}_{\text{SCE}}$ versus OCP at a potential scan rate of 1 mV/s. The EIS measurements were performed in a frequency range from 100 kHz down to 10 mHz at OCP with an applied 10 mV sinusoidal signal amplitude. The impedance data was interpreted by using the Zsimpwin software and equivalent electron circuits.

2.5. Dry wear and corrosive wear testing

The sample size for dry wear and corrosive wear test is $15\text{ mm} \times 15\text{ mm} \times 12\text{ mm}$. Before the experiment, the surfaces of the coatings were polished according to the above procedures. The surface roughness of the samples was measured using a three-dimensional topography measuring instrument (SuperView W1-S100, Chotest Technology Inc., Shenzhen, China) in accordance with the ISO 25178 standard. The dry wear and corrosive wear properties of both coatings and 304 stainless steel were evaluated using a reciprocating wear testing machine (MWF-002, Shandong Baohang Machinery Equipment Manufacturing Co., Ltd., Jinan, China) with normal loads of 30 N and 50 N. The schematic diagram of the device is shown in Fig. 1. Both dry wear and corrosive wear tests use Si_3N_4 balls with a diameter of 6 mm as the friction pair. The test time is 60 min, the reciprocating stroke is 6 mm, the reciprocating frequency is 1 Hz. Corrosive wear performance tests were performed in 3.5 wt% NaCl solution. Before the corrosive wear experiment, the sample

was soaked in 3.5 % NaCl solution for 30 min to obtain a stable open circuit potential. During the experiment, the samples were sealed and installed, leaving only the coating in contact with the corrosive liquid. Three samples were selected for each experimental parameter for repeated testing to ensure the repeatability of the experimental data. The microstructure of the worn coating surface was characterized using field emission scanning electron microscopy equipped with a secondary electron detector (Tescan Mira4, TESCAN GROUP, Czech Republic). The working voltage is 20 keV, and the beam current is 1 nA. The wear volume of both coatings and 304 stainless steel were characterized using a three-dimensional topography measuring instrument (SuperView W1-S100, Chotest Technology Inc., Shenzhen, China). The wear rate (W) was calculated using the following formula:

$$W = V/T$$

$V (\text{mm}^3)$ is the wear volume, and $T (\text{h})$ is the wear time.

3. Results and discussion

3.1. Gas-atomized powders

Fig. 2 shows the X-ray diffraction (XRD) patterns of CoCrFeNiBSiY and FeNiCrCoBSiNb powders. CoCrFeNiBSiY powder is mainly composed of face-centered cubic (FCC) solid solution phase with a small amount of borides. Preliminary research results show that the boride phase is mainly chromium boride and iron boride [27]. FeNiCrCoBSiNb powder is also mainly composed of face-centered cubic solid solution phase and contains a small amount of laves phase. It can be found that both powders exhibit broad halo peaks near the diffraction angle of 45° , indicating that there is a certain amount of nanocrystalline or amorphous phase in both powders. Chong et al. [28] also reported similar research results.

Fig. 3 shows the surface morphologies, cross-sectional morphologies,

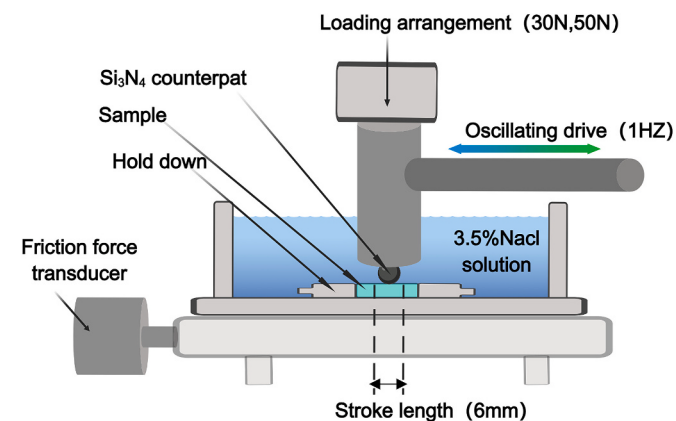


Fig. 1. Schematic diagram of the corrosive wear test.

Table 4

Process parameters for preparing laser cladded coatings.

	Laser power (W)	scanning rate (mm/s)	Powder feeding rate (g/min)	Overlap rate	The width of a single laser cladding layer (mm)	Spot diameter (mm)
CoCrFeNiBSiY	600	5	8.8	50 %	2.8	3
FeNiCrCoBSiNb	600	5	9.3	50 %	2.8	3

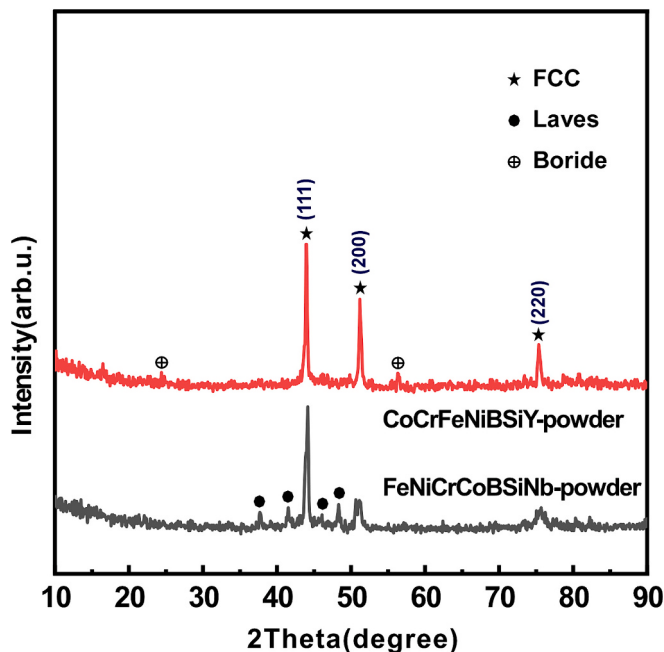


Fig. 2. X-ray diffraction (XRD) patterns of the CoCrFeNiBSiY and FeNiCrCoBSiNb powders.

and particle size distribution histograms of the CoCrFeNiBSiY and FeNiCrCoBSiNb powders. It is obvious that both gas-atomized powders have excellent sphericity. Fig. 3(a1) and (b1) shows that there are a large number of gray stripes inside the CoCrFeNiBSiY powder, while the cross-section of the FeNiCrCoBSiNb powder contains some bright white and gray round spots. Table 5 shows the EDS analysis results of the marked positions in Fig. 3. It can be found that the precipitated phases in both

powders contain high contents of B element respectively. Although the analysis results of the content of B element are not accurate enough, combined with the XRD analysis results in Fig. 2, it can be inferred that borides are generated during the powder preparation process. In order to further characterize the impurity content of the powder, Table 6 lists the nitrogen and oxygen content of CoCrFeNiBSiY and FeNiCrCoBSiNb powders. It was found that the CoCrFeNiBSiY powder contains high oxygen content. The average particle sizes of the CoCrFeNiBSiY and FeNiCrCoBSiNb powders are 74.4 μm and 79.9 μm respectively.

3.2. Phase structure and microstructure of laser cladded coatings

Fig. 4 shows the X-ray diffraction (XRD) patterns of the laser cladded coatings. It can be found that both coatings are mainly composed of FCC solid solution, borides, and a small amount of Laves phase. Compared with the XRD pattern of the powders in Fig. 2, high-intensity diffraction peaks appear in the diffraction angle range of 25°–35°. According to previous research results [27], this may be due to the generation of new boride phases during the laser cladding process. Aguilar-Hurtado et al. [29] also confirmed that the presence of Cr—B, Mn—B, and Fe—B bonds points towards forming (Cr, Fe)₂B borides in the Fe_{50-x}Mn₃₀Co₁₀Cr₁₀B_x multi-component alloys. It can be inferred that the content of borides in the CoCrFeNiBSiY coating is relatively high. In addition, compared with Fig. 3, the diffraction peaks of both coatings near 44° are broadened, which confirms that rapid cooling during laser cladding promotes the

Table 5
EDS analysis results of marked positions in Fig. 3 (at.%).

	Fe	Co	Ni	Cr	B	Si	Y	Nb
1	13.1	16.62	24.70	6.10	25.90	9.58	3.99	–
2	14.12	11.65	5.82	25.46	41.10	1.43	0.43	–
3	35.77	5.03	14.41	6.77	31.51	1.86	–	4.64
4	3.65	0.26	0.45	6.96	81.00	0.17	–	7.50

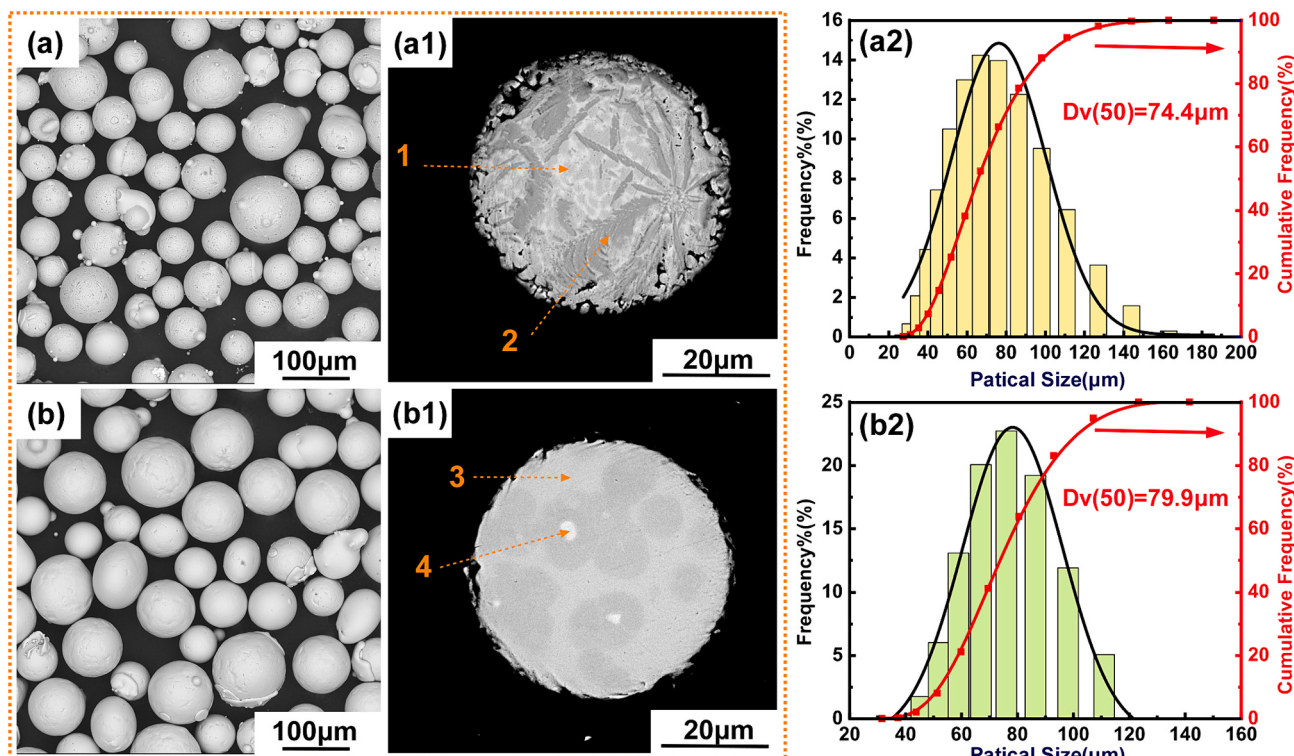


Fig. 3. Backscattered electron images of the surface and cross-sectional morphologies of CoCrFeNiBSiY and FeNiCrCoBSiNb powders, as well as the powder size distribution histograms. (a, a1, a2) CoCrFeNiBSiY powder, (b, b1, b2) FeNiCrCoBSiNb powder.

Table 6

Nitrogen and oxygen content of the CoCrFeNiBSiY and FeNiCrCoBSiNb powders.

	Oxygen content	Nitrogen content
CoCrFeNiBSiY powder	510 ppm	27 ppm
FeNiCrCoBSiNb powder	92 ppm	23 ppm

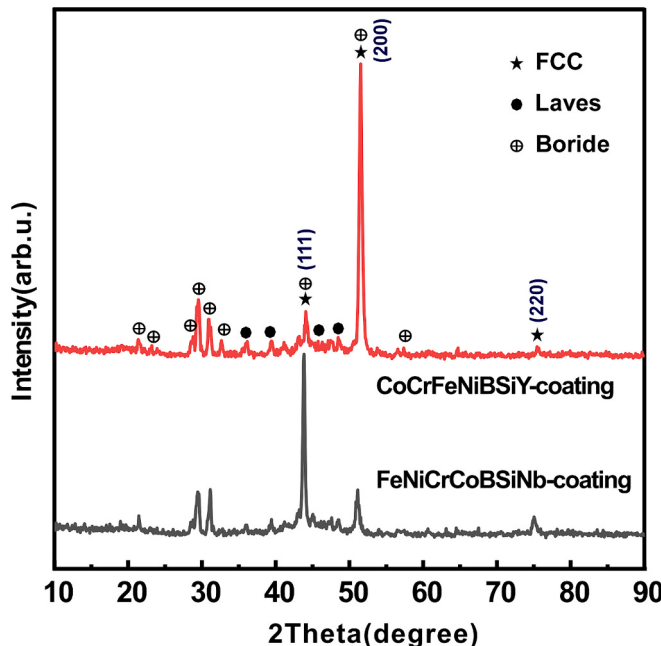


Fig. 4. X-ray diffraction patterns of the CoCrFeNiBSiY and FeNiCrCoBSiNb laser cladded coatings.

generation of nanocrystals and even amorphous phases. This phenomenon is similar to the research results of Wang et al. [30] and Huang et al. [31].

Fig. 5 illustrates the cross-sectional morphologies of laser cladded CoCrFeNiBSiY and FeNiCrCoBSiNb coatings. It can be seen from Fig. 5 (a) and (b) that the microstructure of both coatings is relatively uniform and dense. Both coatings contain a small number of dispersed fine pores. Coatings exhibit good metallurgical bonding with the substrate. The average thicknesses of CoCrFeNiBSiY and FeNiCrCoBSiNb coatings are approximately 0.9 ± 0.15 mm and 0.8 ± 0.12 mm, respectively.

It was found that the two coatings exhibited distinct microstructures. Fig. 5(a1) and (b1) shows that thick dendrites perpendicular to the direction of the substrate are formed in the bonding area between the two coatings and the 304 stainless steel substrate. The size of the dendrites formed in the CoCrFeNiBSiY coating is significantly larger, indicating that the component segregation is more serious. This may also be related to the precipitation of more boride phases. As shown in Fig. 5(a2) and (b2), the dendritic structures in the middle regions of both cladding layers are significantly refined. This may be related to the faster heat dissipation speed and heat dissipation direction of the molten pool. Fig. 5(a3) shows that gray strips appear on the top of the CoCrFeNiBSiY coating, which is similar to the cross-sectional morphology of the powder. Two pattern-like structures with different morphologies appeared on the top of the FeNiCrCoBSiNb coating, as shown in Fig. 5 (b3). Table 7 shows the EDS analysis results of the marked positions in Fig. 5. Comparing with Table 5, it is found that the chemical composition of the surface layers of both coatings is basically consistent with the composition of the corresponding powders.

In order to characterize the component segregation, the EDS analysis results of the area near the top of the cross-section of both coatings are shown in Fig. 6, respectively. In the CoCrFeNiBSiY coating, the Cr

element is concentrated in the gray strips. Si and Y are concentrated in bright white areas. The distribution of Fe, Ni, and Co elements outside the gray strips is relatively uniform. Combined with the XRD analysis results in Fig. 4, it can be inferred that the gray strip area in Fig. 6(a) is composed of Cr- and Fe-rich borides. However, the difference is that the elements in the FeNiCrCoBSiNb coating are evenly distributed without obvious segregation (Fig. 6(b1)). In addition, EDS analysis results show that the chemical composition on top of both coatings is very close to the nominal composition of the corresponding powders (Table 1).

3.3. Microhardness of laser cladded coatings

Fig. 7 shows the microhardness distribution and average microhardness of both laser cladded coatings. The microhardness distribution of the two laser cladded coatings is relatively uniform. Due to the dilution effect of 304 stainless steel, there is a transition zone between the coating and the substrate, and the microhardness decreases slightly. The average microhardness of CoCrFeNiBSiY and FeNiCrCoBSiNb coatings are 578.6 and 632.5 (HV_{0.2}) respectively, which is approximately 3 times that of 304 stainless steel. Table 8 lists the microhardness of some laser cladded high-entropy alloy coatings reported in the literatures. The microhardness of FeCoCrNi, FeCoCrNiMn, and FeCoCrNiCu bulk high-entropy alloys reported in the literatures is approximately 209, 188, and 375 HV respectively [32,33]. It can be found that the microhardness of both coatings in this study is higher than that of bulk high-entropy alloys with FCC structure such as FeCoCrNi. The main reason is due to the precipitation of strengthening phases such as borides and solid solution strengthening caused by lattice distortion [34–36].

3.4. Corrosion resistance of laser cladded coatings

Fig. 8(a) displays the potentiodynamic polarization curves of both coatings and 304 stainless steel in 3.5 wt% NaCl solution at room temperature. A series of kinetic parameters derived from the polarization curves are shown in Table 9. E_{corr} , I_{corr} , and I_{pass} represent corrosion potential, corrosion current density, and passivation current densities, respectively. It can be found that the CoCrFeNiBSiY coating has the highest corrosion potential, while 304 stainless steel has the lowest corrosion current. In general, a high corrosion potential indicates that the material has high chemical stability, while a low corrosion current indicates that the material has a low tendency to be corroded [39]. It can be clearly found that all the potentiodynamic polarization curves contain a passivation platform, indicating that all materials have obvious passivation tendencies. The CoCrFeNiBSiY coating has a low passivation current density, indicating that the coating has excellent corrosion resistance.

Fig. 8(b)-(d) illustrates the Nyquist curves and Bode plots of both coatings and 304 stainless steel in 3.5 wt% NaCl solution with the electrical equivalent circuit (EEC) used for fitting the EIS experimental data. It is apparent that all the impedance spectrums are characterized by a similar single capacitive arc. Earlier studies have linked the capacitive arc to the dissolution of the metal and proved that the larger the diameter of the capacitive arc, the greater the impedance of the system and the better the corrosion resistance [40]. 304 stainless steel has the largest capacitive arc radius, and its excellent corrosion resistance may be attributed to its single-phase structure. According to Fig. 8 (c), the slopes of the log Z-log f curves of both coatings and 304 stainless steel are close to -1 , indicating the pseudocapacitive characteristic of the passive film formed on the alloys. In addition, only a single phase angle peak can be clearly observed on the Bode diagram (Fig. 8(d)), that is, one relaxation time constant, indicating that the equivalent circuit includes a pair of series-parallel circuits. Therefore, a simple Randles equivalent circuit $R_s(Q_{film}R_{film})$ is employed to fit the experimental data, as shown in Fig. 8b. In this model, R_s represents the resistance of the solution and is affected by the ionization of metal ions on the alloy surface. A passivation film and an electric double layer exist at the

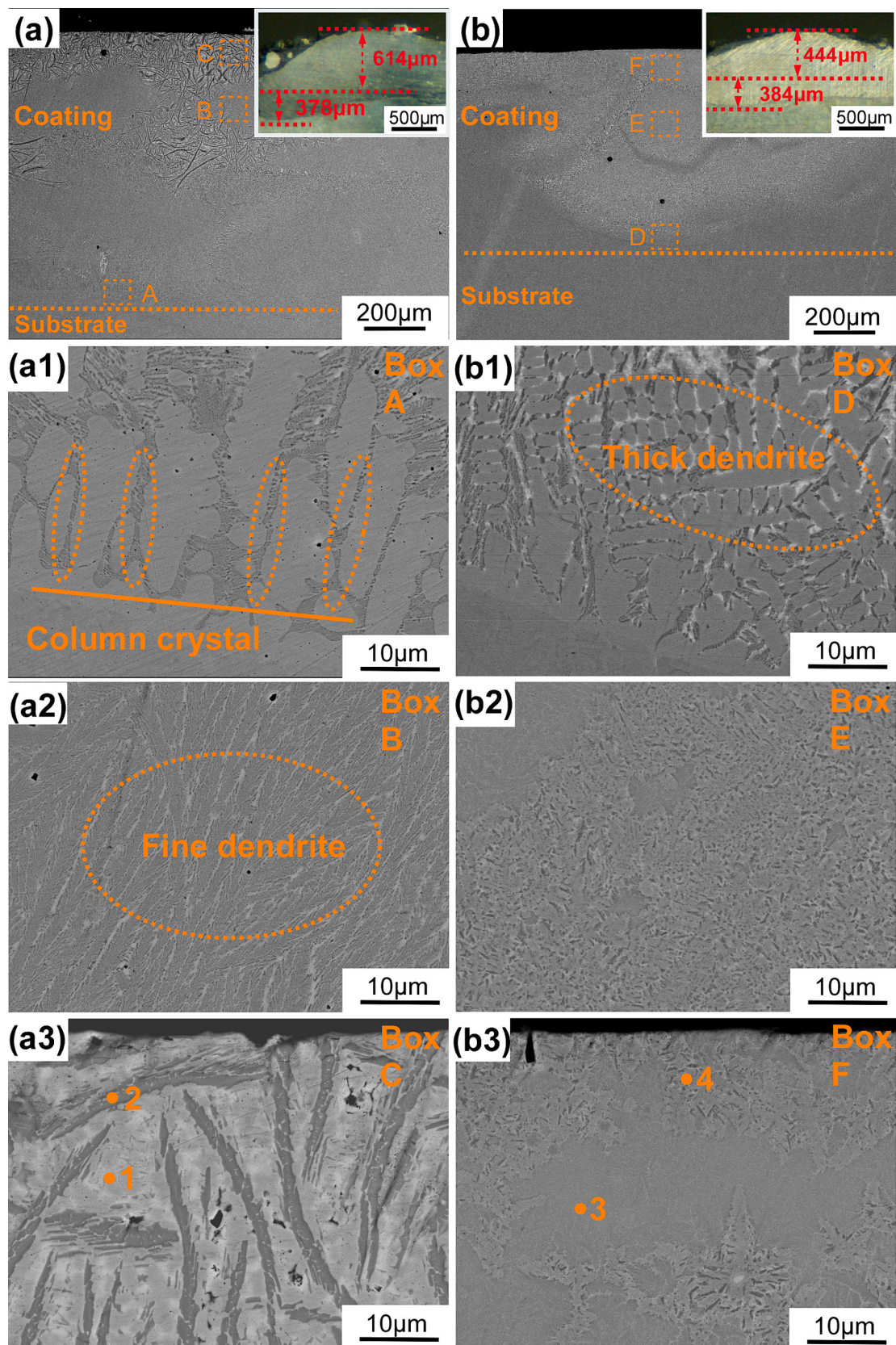


Fig. 5. Backscattered electron images of cross-sectional morphologies of CoCrFeNiBSiY (a, a1, a2, a3) and FeNiCrCoBSiNb (b, b1, b2, b3) coatings. (a1, a2, and a3 correspond to areas A, B, and C in Fig. 5a, respectively. b1, b2, and b3 correspond to the D, E, and F areas in Fig. 5b, respectively.)

Table 7
EDS analysis results of marked positions in Fig. 5 (at.%).

	Fe	Co	Ni	Cr	Si	Y	Nb
1	15.91	22.54	36.27	8.08	11.38	5.82	–
2	22.16	14.62	4.55	58.13	0.53	0.35	–
3	56.50	6.05	18.10	12.68	1.65	–	5.01
4	56.24	5.88	19.50	11.82	1.95	–	4.60

electrode/electrolyte solution interface, and R_{film} represents the total resistance of the passivation film and the electric double layer. Studies have shown that the passivation film has a high charge transfer resistance, and the charge transfer resistance value mainly depends on the passivation film [41]. The lower the R_{film} value, the easier it is for the charge to pass through the passivation film. Equivalent capacitance Q_{film} (constant phase angle element CPE) is used for fitting instead of pure capacitance C. These fitting parameters are also shown in Table 9. The Chi-squared (χ^2) value is related to the fitting accuracy. The order of magnitude of χ^2 values for both coatings and 304 stainless steel is 10^{-3} ,

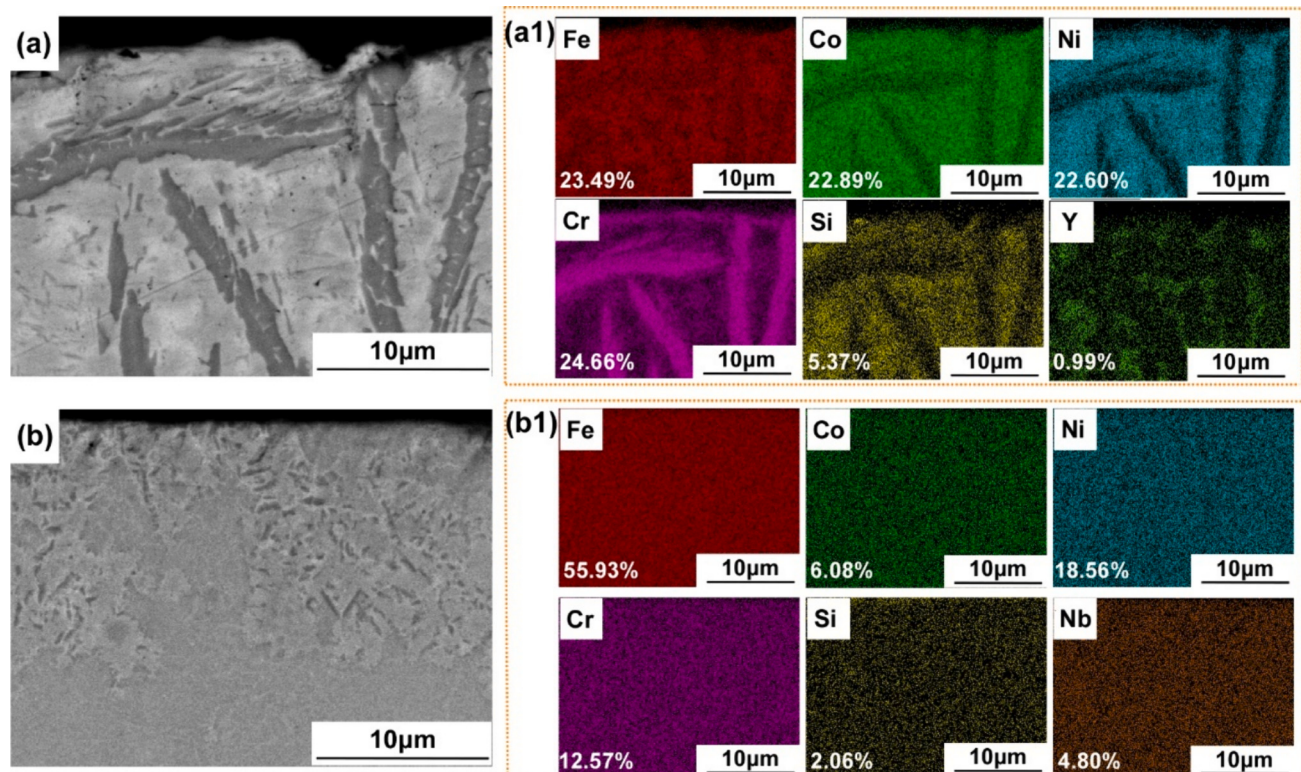


Fig. 6. EDS analysis results of CoCrFeNiBSiY and FeNiCrCoBSiNb laser cladded coatings. (a) backscattered electron image of the CoCrFeNiBSiY coating, (a1) elemental distribution of the CoCrFeNiBSiY coating, (b) backscattered electron image of the FeNiCrCoBSiNb coating, (b1) elemental distribution of the FeNiCrCoBSiNb coating.

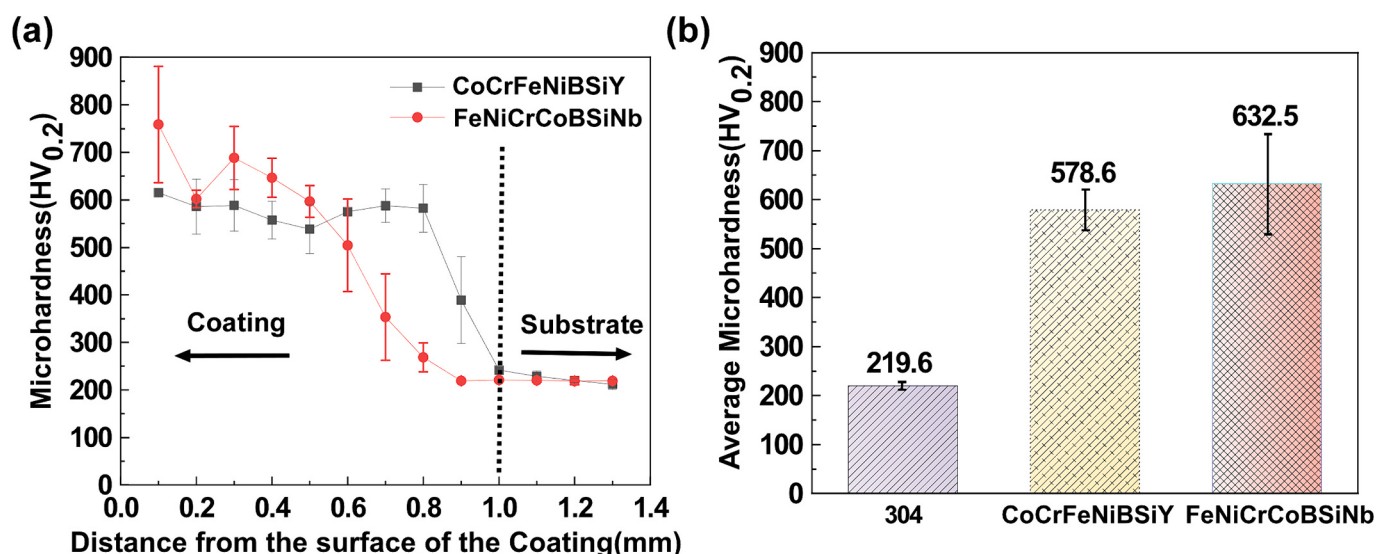
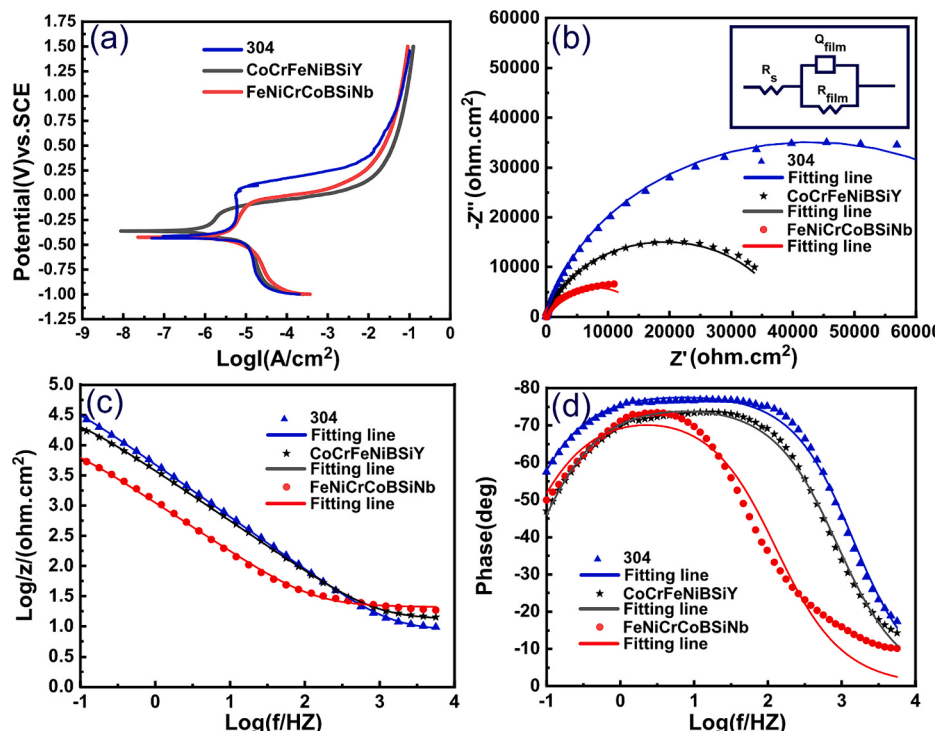


Fig. 7. (a) Microhardness distribution and (b) average microhardness of the CoCrFeNiBSiY and FeNiCrCoBSiNb laser cladded coatings.

Table 8

Microhardness of high-entropy alloy coatings in this work and literature reports.

HEA coating	Preparation process	Phases	Microhardness (HV)	Authors
CoCrFeNiBSiY	Laser cladding	FCC + Laves+Boride	578.6	This study
FeNiCrCoBSiNb	Laser cladding	FCC + Laves+Boride	632.5	This study
Fe ₂₅ Co ₂₅ Cr ₂₅ Ni ₂₅	Laser cladding	FCC	209	Ma et al. [32]
Fe ₂₀ Co ₂₀ Cr ₂₀ Ni ₂₀ Mn ₂₀	Laser cladding	FCC	188	Ma et al. [32]
Fe ₂₀ Co ₂₀ Cr ₂₀ Ni ₂₀ Cu ₂₀	Laser cladding	FCC	375	Zhang et al. [33]
Fe ₂₅ Co ₂₅ Ni ₂₅ (B _{0.7} Si _{0.3}) ₂₅	Laser cladding	FCC + Boride	587.1	Cheng et al. [37]
Ni _{1.5} CrCoFe _{0.5} Mo _{0.1} Nb _{0.55}	Laser cladding	FCC + Laves	573.5	Wen et al. [35]
Cr ₂₀ Cu ₂₀ Fe ₂₀ Ni ₂₀ Al ₂₀	Plasma cladding	BCC	429.2	Wang et al. [38]

**Fig. 8.** (a) Potentiodynamic polarization curves, (b) Nyquist and (c, d) Bode plots of the laser cladded FeCoNiCrBSiY coating and FeCoNiCrBSiNb coating in 3.5 wt% NaCl solution at room temperature.**Table 9**

A series of electrochemical parameters fitted from the potentiodynamic polarization and EIS curves.

	E_{corr} (mV)	I_{corr} ($A \cdot cm^{-2}$)	I_{pass} ($A \cdot cm^{-2}$)	R_s ($ohm \cdot cm^2$)	$Q_{film} \cdot Y_0$ ($\Omega^{-1} \cdot cm^{-2} \cdot s^{-n}$)	$Q_{film} \cdot n$	R_{film} ($ohm \cdot cm^2$)	χ^2
304	-427	8.58×10^{-8}	6.28×10^{-6}	8.478	4.192×10^{-5}	0.8724	85,810	1.43×10^{-3}
CoCrFeNiBSiY coating	-395	5.63×10^{-7}	1.65×10^{-6}	12.87	5.553×10^{-5}	0.8409	38,610	1.33×10^{-3}
FeNiCrCoBSiNb coating	-409	2.22×10^{-6}	6.60×10^{-6}	20.72	1.963×10^{-4}	0.8221	15,610	9.28×10^{-3}

indicating that it is reasonable to use the $R_s(Q_{film}R_{film})$ equivalent circuit to fit the EIS data in this study. It is reported in the literature that the capacitance of the passivation film on the coating can be represented by the equivalent capacitance Q [42]. Q includes the constant Y_0 and dimensionless exponent n . n is the deviation value from pure capacitive behavior. The closer the system is to an ideal capacitor, the closer the value of n is to 1 [43]. It can be found from Table 9 that the $Q_{film} \cdot Y_0$ value of 304 stainless steel is smaller, indicating that the passivation film formed on its surface is thicker and denser. In addition, the $Q_{film} \cdot Y_0$ value of CoCrFeNiBSiY coating is very close to that of 304 stainless steel. The high R_{film} value of 304 stainless steel indicates that its surface passivation film is stable and less sensitive to anions in solution. In our previous work, XPS analysis was conducted on the passivation film on the surface of the corroded CoCrFeNiBSiY and FeNiCrCoBSiNb coatings [27]. The results show that the passivation film formed on the surface of

the FeCoNiCrBSiY coating contains high content of Cr oxide or hydroxide, which is beneficial to improve its compactness and stability. The Cr/Fe ratio of the passivation film is 1.8, which is significantly higher than 0.15 of the FeNiCrCoBSiNb coating.

3.5. Dry wear and corrosive wear resistance of laser cladded coatings and 304 stainless steel

Before the wear experiment, the initial surfaces roughness (S_a) of the CoCrFeNiBSiY and FeNiCrCoBSiNb coatings and 304 stainless steel were $0.175 \pm 0.042 \mu m$, $0.225 \pm 0.028 \mu m$ and $0.145 \pm 0.037 \mu m$, respectively. Fig. 9 shows the friction coefficient curves of both coatings and 304 stainless steel under dry wear and corrosive wear conditions. It can be inferred that the dry wear and corrosive wear processes are mainly divided into two stages: the running-in period and the stable period.

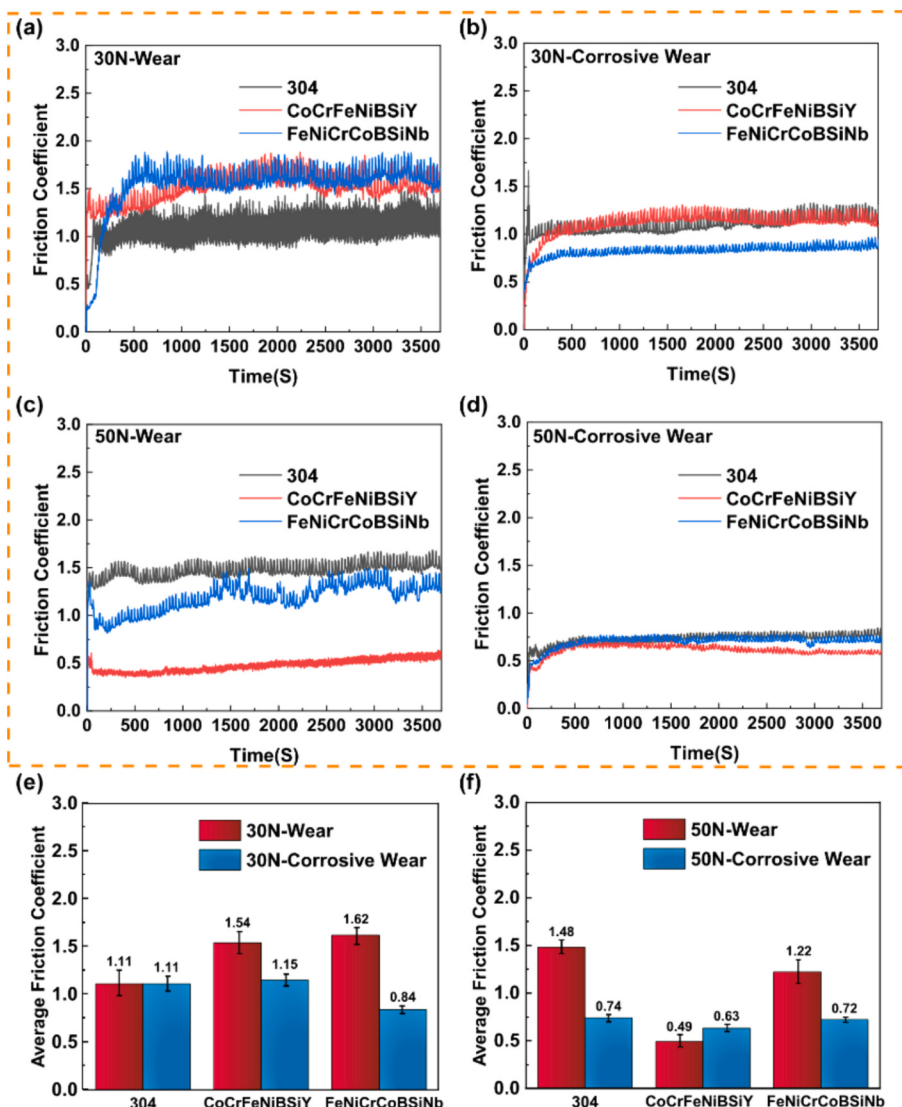


Fig. 9. Friction coefficients of CoCrFeNiBSiY and FeNiCrCoBSiNb coatings and 304 stainless steel under dry wear and corrosive wear conditions. (a) under dry wear condition with a normal load of 30 N, (b) under corrosive wear condition with a normal load of 30 N, (c) under dry wear condition with a normal load of 50 N, (d) under corrosive wear condition with a normal load of 50 N, (e) average friction coefficient under 30 N load, (f) average friction coefficient under 50 N load.

Literature research shows that the friction coefficient rises rapidly due to the surface roughness of the cladding coatings during the running-in stage [44,45]. As the reciprocating cycles increase, the particles are continuously peeled off during the dry wear process. Wear debris with a blocking effect is formed between the cladding layer surface and the friction pair. The wear debris undergoes an oxidation reaction during the friction process to form a friction layer with a friction-reducing effect. The friction coefficient tends to be stable. However, during the corrosive wear process, the friction coefficient of both coatings and 304 stainless steel is mainly affected by the passivation film generated on its surface.

The average friction coefficients of both coatings and 304 stainless steel under dry wear and corrosive wear conditions with normal loads of 30 N and 50 N are shown in Fig. 9(e) and (f) respectively. Under 30 N dry wear conditions, the average friction coefficients of the CoCrFeNiBSiY and FeNiCrCoBSiNb coatings are 1.54 and 1.62 respectively, which are both higher than 1.11 of 304 stainless steel. When the load increases to 50 N, the average friction coefficients of the CoCrFeNiBSiY and FeNiCrCoBSiNb coatings decrease to 0.49 and 1.22, respectively. According to Cao et al. [26], the friction coefficient is related to the strength of the material, friction load, and contact area. Under other

conditions being equal, the friction coefficient decreases as the load increases. However, as the load increases, the average friction coefficient of 304 stainless steel has increased to 1.48. This may be due to the low hardness of 304 stainless steel. Literature research showed that the surface of 304 stainless steel is prone to adhesive wear under high-temperature conditions as the load increases, resulting in a rougher surface [46].

In the corrosive environment, the friction coefficient of 304 stainless steel under a 30 N load remains almost unchanged compared to that under dry wear condition. However, the friction coefficients of both coatings decreased significantly. When the load increases to 50 N, the friction coefficients of corrosive wear of all materials continue to decrease significantly compared with the case of 30 N. In addition, the friction coefficient of CoCrFeNiBSiY coating is the lowest. It can be found that the friction coefficient of the CoCrFeNiBSiY coating under corrosive wear is slightly higher than that under dry wear with a normal load of 50 N. This is mainly because there are significant differences in the failure mechanisms of materials under dry wear and corrosive wear conditions. Under dry friction conditions, oxidative wear mainly occurs on the material surface. However, the passivation film formed on the material surface during corrosive wear is mainly controlled by its

corrosion behavior. In addition, it can be clearly found that the friction coefficient curves of all materials under corrosion conditions are significantly smoother and more stable than those under dry friction conditions.

Fig. 10 shows the volume wear rates of both coatings and 304 stainless steel under different loads. As can be seen from Fig. 10(a), the volume wear rates of CoCrFeNiBSiY and FeNiCrCoBSiNb coatings under dry wear conditions are 0.35 times and 0.31 times that of 304 stainless steel, respectively. When the load increases to 50 N, the volume wear rate of 304 stainless steel increases by 24 %. The volume wear rates of CoCrFeNiBSiY and FeNiCrCoBSiNb coatings are 0.46 times and 0.32 times that of 304 stainless steel, respectively. Under dry wear condition with a normal load of 30 N, it can be found that the wear rate of both coatings and 304 stainless steel is close to an inverse relationship with their microhardness, indicating that hardness is the main factor affecting the wear resistance. In addition, the wear resistance of FeNiCrCoBSiNb coatings with high hardness is less sensitive to load.

In corrosive wear environments, the volume wear rates of both coatings and 304 stainless steel under 30 N and 50 N conditions are significantly smaller than those under dry wear. Hua et al. [25] also reported similar results. This shows that the influence of corrosion behavior on the corrosive wear process cannot be ignored. Under a load of 30 N, the volume loss rate of corrosive wear of 304 stainless steel is only 0.29 times that of dry wear. The volume wear rates of CoCrFeNiBSiY and FeNiCrCoBSiNb coatings are only 0.37 times and 0.63 times that of 304 stainless steel, respectively. When the load increases to 50 N, the volume wear rate of corrosive wear of 304 stainless steel increases by 144 %. The volume wear rates of CoCrFeNiBSiY and FeNiCrCoBSiNb coatings are 0.35 times and 0.5 times that of 304 stainless steel, respectively. This shows that the corrosive wear resistance performance of 304 stainless steel is very sensitive to load, while the sensitivity of both coatings to load is significantly reduced. Although the microhardness of CoCrFeNiBSiY is slightly lower than that of FeNiCrCoBSiNb coating, the corrosive wear resistance of CoCrFeNiBSiY coating is significantly better than that of FeNiCrCoBSiNb coating and 304 stainless steel. This also shows that the corrosion behavior of the material significantly affects its corrosive wear resistance properties.

The friction coefficient is closely related to the surface morphologies of the materials. Fig. 11 shows the morphologies of the wear scars of both coatings and 304 stainless steel under dry wear and corrosive wear conditions with a load of 30 N. Table 10 gives the EDS analysis results of the marked positions in Fig. 11. As can be seen from Fig. 11(a), oxides appear on the surface of 304 stainless steel under dry wear conditions. The oxide layer is discontinuous and has cracks in multiple directions internally, causing the oxide layer to peel off in an obvious layered manner. This can be inferred that the oxide layer formed during the friction process has weak binding force with the 304 stainless steel substrate. EDS analysis results show that these oxides are mainly

enriched in Fe and Cr. It can be found that the position marked 2 in Fig. 11(a) contains a high Fe/Cr ratio. Bateni et al. [46] also reported that the wear mechanism of 304 stainless steel is mainly the delamination and spalling of the oxide layer.

As can be seen from Fig. 11(b), the surface of the CoCrFeNiBSiY coating after dry wear is relatively rough. The oxide layer is relatively dense and continuous. No penetrating cracks or layered peeling phenomena are found. However, the oxide layer falls off in the form of wear debris. This can be inferred that the oxide layer formed on the surface of the coating is thicker and better combined with the substrate. Table 10 shows that the oxide layer is enriched in Cr, Fe, Co, and Ni elements. The ratio of Fe/(CoCrNi) is only about 0.4. As shown in Fig. 11(c), a phenomenon similar to that of 304 stainless steel appears on the surface of CoCrFeNiBSiNb coating. EDS analysis results show that the oxide layer formed on the coating surface is mainly enriched in Cr, Fe, and Ni. The content of alloy elements in the oxide layer is higher than that of 304 stainless steel, but the Fe/(CoCrNi) ratio is also significantly high (>1.5). It can be inferred that the increase in alloying elements is conducive to increasing the compactness of the oxide layer on the coating surface as well as its bonding force with the coating. The oxide layer formed on the surface of the coatings peels off in the form of fragments, resulting in an increase in the roughness of the coating surface. This is also the reason why the dry wear coefficient of both coatings is higher than that of 304 stainless steel.

It can be seen from Fig. 11(d)(e)(f) that the wear scar morphologies of both coatings and 304 stainless steel after corrosive wear are obviously smoother than those under dry wear conditions. This phenomenon is consistent with the low friction coefficient under corrosive wear conditions for all materials. Obvious corrosion products can be found on the surfaces of all materials. Typical wear morphologies such as furrows appear. This confirmed that an obvious corrosion process occurred on the material surface and the wear mechanism was mainly abrasive wear. This result is similar to the studies by Feng et al. [23] and Ji [47] et al. On the surface of 304 stainless steel (Fig. 11(d)), the bright white area (location marked 7) obviously has a higher oxide content, mainly composed of Fe and Cr oxides. However, the composition of the gray area (location marked 8) is almost consistent with the composition of the 304 stainless steel substrate, indicating that part of the surface passivation film has been removed due to wear. Fig. 11(e) and (f) show that a continuous dense oxide layer is formed on the surface of both coatings after corrosive wear. The oxide layer formed on the surface of the CoCrFeNiBSiY coating is thicker. EDS analysis results show that the Fe/(CoCrNi) ratio of the oxide layer on the CoCrFeNiBSiY coating is only about 0.3. Although the oxide layer on the surface of the CoCrFeNiBSiNb coating also cracked, repassivation obviously occurred in the pits. The oxide layer on the surface of the CoCrFeNiBSiNb coating is relatively dense. The Fe/(CoCrNi) ratio of the oxide layer is about 1.5.

Fig. 12 shows the wear scar morphologies of both coatings and 304

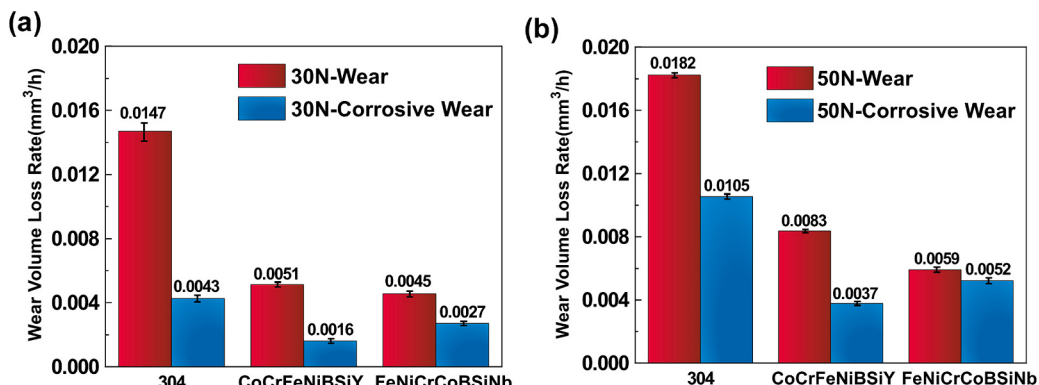


Fig. 10. Volume wear rates of the CoCrFeNiBSiY and FeNiCrCoBSiNb coatings and 304 stainless steel under dry wear and corrosive wear conditions with a normal load of (a) 30 N and (b) 50 N.

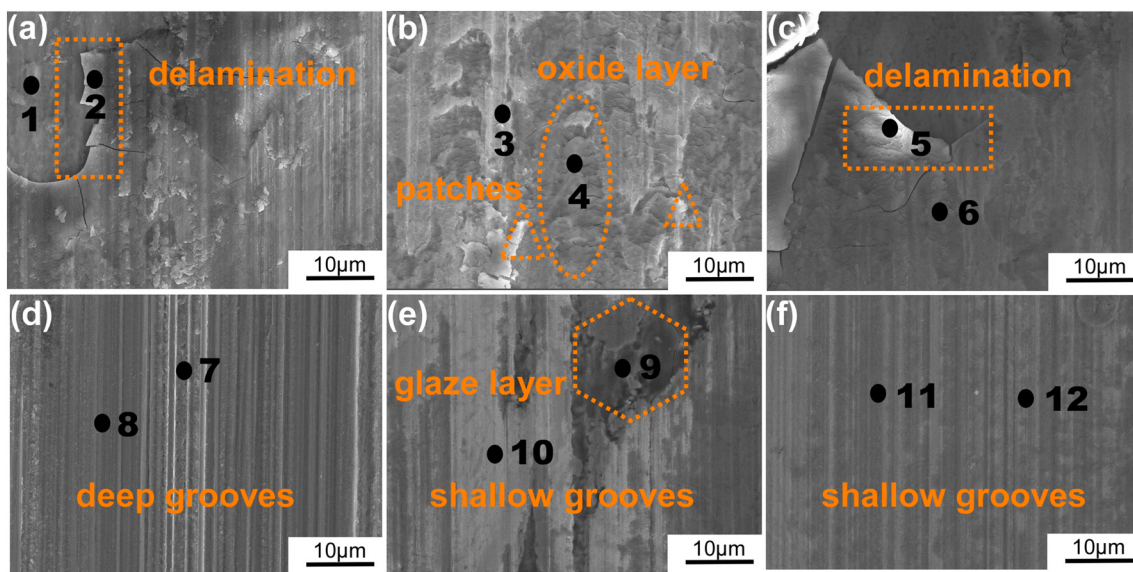


Fig. 11. Secondary electron images of surface morphologies of CoCrFeNiBSiY and FeNiCrCoBSiNb coatings and 304 stainless steel suffered dry wear and corrosive wear with a normal load of 30 N. (a) 304 stainless steel suffered dry wear, (b) CoCrFeNiBSiY coating suffered dry wear, (c) FeNiCrCoBSiNb coating suffered dry wear, (d) 304 stainless steel suffered corrosive wear, (e) CoCrFeNiBSiY coating suffered corrosive wear, (f) FeNiCrCoBSiNb coating suffered corrosive wear.

Table 10
EDS analysis results of marked positions in Fig. 11 (at.%).

Materials	Marked location	O	Si	Cl	Cr	Mn	Fe	Co	Ni	Y	Nb	Mo
304	1	28.63	1.55	–	14.15	0.57	49.85	–	5.19	–	–	0.05
304	2	62.5	4.75	–	6.71	0.32	23.34	–	2.38	–	–	0
CoCrFeNiBSiY	3	16.11	4.52	–	31.38	–	19.03	14.87	12.95	1.14	–	–
CoCrFeNiBSiY	4	39.47	7.03	–	11.20	–	15.03	13.28	13.44	0.55	–	–
FeNiCrCoBSiNb	5	64.04	7.78	–	4.15	–	16.21	1.66	4.86	–	1.31	–
FeNiCrCoBSiNb	6	14.25	1.76	–	11.90	–	48.51	4.76	14.59	–	4.24	–
304	7	26.42	1.05	0.14	16.16	0.53	49.98	–	5.44	–	–	0.28
304	8	9.43	0.81	0.28	16.80	0.71	63.77	–	8.13	–	–	0.08
CoCrFeNiBSiY	9	43.96	11.03	0.39	11.55	–	11.57	11.03	9.76	0.71	–	–
CoCrFeNiBSiY	10	2.42	8.23	0	17.63	–	19.73	21.15	27.24	3.60	–	–
FeNiCrCoBSiNb	11	18.45	2.26	0.04	11.32	–	45.17	4.55	15.66	–	2.55	–
FeNiCrCoBSiNb	12	6.28	1.6	0	11.76	–	51.58	5.56	17.60	–	5.62	–

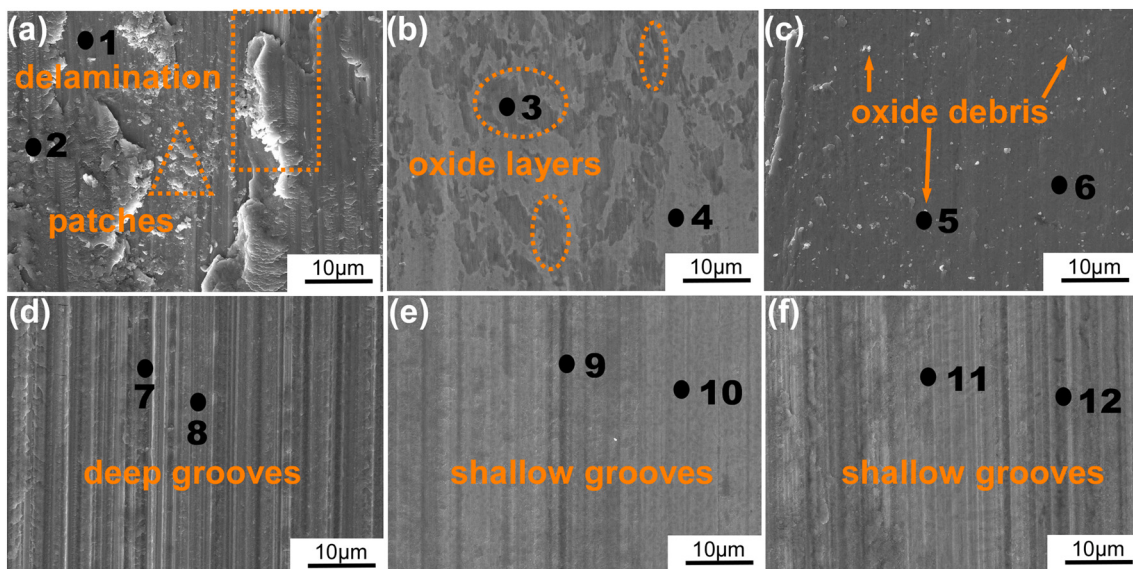


Fig. 12. Secondary electron images of surface morphologies of CoCrFeNiBSiY and FeNiCrCoBSiNb coatings and 304 stainless steel suffered dry wear and corrosive wear under 50 N load. (a) 304 stainless steel suffered dry wear, (b) CoCrFeNiBSiY coating suffered dry wear, (c) FeNiCrCoBSiNb coating suffered dry wear, (d) 304 stainless steel suffered corrosive wear, (e) CoCrFeNiBSiY coating suffered corrosive wear, (f) FeNiCrCoBSiNb coating suffered corrosive wear.

stainless steel after dry wear and corrosive wear with a normal load of 50 N. Table 11 shows the EDS analysis results of the marked positions in Fig. 12. Comparing to Fig. 11, it can be found that the increase in friction load significantly changes the morphologies of the oxide layer formed on the surface of all materials after dry wear. As the load increases, the oxide layer formed on the surface of 304 stainless steel becomes thicker. However, the cracking of the oxide layer becomes more serious and the surface becomes rough and uneven. Fig. 9 shows that the friction coefficient of 304 stainless steel under dry wear conditions also increases significantly as the load increases. EDS analysis results show that the Fe/Cr ratio of the oxide layer has almost no change compared with the condition under 30 N load. However, the oxide layer formed on the surface of the CoCrFeNiBSiY coating becomes denser as the load increases. The oxide layer did not break as a whole, only a thin layer peeled off. The oxide layer on the surface of the FeNiCrCoBSiNb coating is dense, but there are more fine oxide debris on the coating surface. According to Fig. 9, it can be found that the dry friction coefficients of both coatings under 50 N wear conditions are significantly lower than that of 304 stainless steel. This phenomenon shows that the morphology of wear scars has a very important influence on the friction coefficient. The EDS analysis results in Table 11 show that the Fe/(CoCrNi) ratio of the oxide layer formed on the CoCrFeNiBSiY coating is about 0.4, which is almost unchanged compared with the case under 30 N load. The Fe/(CoCrNi) ratio of the surface oxide layer of FeNiCrCoBSiNb coating is about 1.6, which is slightly higher than that under 30 N load.

Comparing with Fig. 11(d), it is found that the wear scar morphology of 304 stainless steel after corrosive wear under 50 N load did not change significantly compared with the wear scar morphology under 30 N load. However, the wear scar morphology of the CoCrFeNiBSiY coating after corrosive wear under 50 N load is smoother and denser, without obvious cracks and pits. As the load increases from 30 N to 50 N, the Fe/(CoCrNi) ratio of the surface oxide layer formed on the CoCrFeNiBSiY coating increases from 0.3 to 0.6. Differently, the morphology of the wear scars on the FeNiCrCoBSiNb coating surface still shows typical furrows. The depth and width of the furrow increased. In addition, the Fe/(CoCrNi) ratio of the oxide layer formed on the surface of the FeNiCrCoBSiNb coating increased from 1.5 to 1.7.

4. Discussion

4.1. Microstructural evolution of coatings and its effect on microhardness

According to relevant research reports [26], the microstructural morphologies of laser cladding coatings are mainly determined by the temperature gradient (G) and solidification rate (R) of different areas in the molten pool. In the early stage of solidification, the solid-liquid interface of the molten pool close to the substrate has a slow heat dissipation speed and a small temperature gradient, so the solidification speed is slow and the components are easily supercooled. Normally, nucleation occurs at the solid-liquid interface based on the incompletely melted crystal grains in the substrate. Due to component segregation,

dendrites growing perpendicular to the solid-liquid interface are formed. This is consistent with the microstructure characteristics found in Fig. 5(a1) and (b1). As the solidification process proceeds, the heat dissipation speed in the area near the center of the molten pool accelerates, and the temperature gradient gradually increases. The degree of supercooling at the front edge of the solid-liquid interface increases, resulting in an increase in the nucleation and solidification rates. Therefore, the size of dendrites becomes smaller and gradually transforms into equiaxed grains. This may be the reason why the dendrite size becomes smaller and equiaxed grains appear in Fig. 5(a2) and (b2). In the top area of the CoCrFeNiBSiY coating, the faster cooling rate results in a larger degree of supercooling at the front edge of the solid-liquid interface. The precipitated boride rapidly nucleates and grows into dendrites along the preferential growth direction. The growth rate of dendrite arms is faster along the direction of large temperature gradient. And due to the disturbance of the molten pool, “wicker-like” dendrites with curved morphology are formed. In the research report by Zhang et al. [34], borides such as $(\text{Fe}, \text{Cr})_2\text{B}$ penetrated the entire coating in a stripe manner.

XRD analysis results show that both coatings are mainly composed of FCC solid solution, borides, and a small amount of Lavas phase. Zhang et al. [22] reported that the microhardness of coatings with boride reinforcement phases can reach >650 HV. According to literature reports, the microhardness of FeCoCrNi and FeCoCrNiMn high-entropy alloys with FCC structure is only about 209 and 188 HV, respectively [32,33]. The microhardness of CoCrFeNiBSiY and FeNiCrCoBSiNb coatings in this study are 578.6 HV and 632.5 HV, respectively. Both coatings exhibit high hardness mainly due to the precipitation of strengthening phases and the solid solution strengthening. According to relevant research reports [26,48], high mixing entropy can promote the mutual solubility of elements and form a solid solution structure. The atomic sizes of the Fe (0.1241 nm), Cr (0.1249 nm), Ni (0.1246 nm), and Co (0.1251 nm) elements are similar and the atomic binding energy between each atom is small. The probability of elements occupying each node position of the crystal lattice is similar, which is also conducive to the formation of a simple solid solution structure [49]. During the laser cladding process, the powder quickly reaches a superheated state. Faster cooling rates cause the alloy to tend to form a supersaturated solid solution. This phenomenon is similar to the results reported by Cheng et al. [37] and Ma et al. [50].

4.2. Dry wear mechanism of laser cladded coatings and 304 stainless steel

Typically, the wear resistance of metallic materials is related to hardness and elastic modulus. According to Archard's wear law [51], the wear resistance of metallic materials is directly proportional to their hardness. Fig. 13 illustrates the schematic diagram of dry wear and corrosive wear mechanisms of CoCrFeNiBSiY coating and 304 stainless steel. Under a load of 30 N, there are a large number of cracks in the oxide layer formed on the surface of 304 stainless steel, and lamellar peeling occurs, as shown in Fig. 13(a). EDS analysis results show that the

Table 11
EDS analysis results of marked positions in Fig. 12 (at.%).

Materials	Marked location	O	Si	Cl	Cr	Mn	Fe	Co	Ni	Y	Nb	Mo
304	1	3.90	1.05	–	19.30	0.85	67.78	–	7.13	–	–	0
304	2	37.96	3.94	–	11.91	0.55	41.36	–	4.25	–	–	0.04
CoCrFeNiBSiY	3	49.33	4.46	–	15.86	–	13.01	8.47	7.99	0.88	–	–
CoCrFeNiBSiY	4	4.66	4.50	–	27	–	24.84	19.73	18.84	0.84	–	–
FeNiCrCoBSiNb	5	24.97	1.55	–	11.04	–	43.43	3.75	11.88	–	3.27	–
FeNiCrCoBSiNb	6	4.68	1.42	–	13.99	–	56.10	4.96	15.37	–	3.49	–
304	7	12.16	1.2	0.02	18.11	0.84	61.39	–	6.16	–	–	0.11
304	8	30.52	2.08	0.06	14.85	0.65	46.52	–	5	–	–	0.32
CoCrFeNiBSiY	9	21.81	3.85	0.07	22.19	–	26.10	12.55	12.32	1.11	–	–
CoCrFeNiBSiY	10	13.68	4.67	0.02	18.74	–	30.89	15.51	16.32	0.38	–	–
FeNiCrCoBSiNb	11	3.52	1.43	0.04	14.76	–	58.77	4.11	15.03	–	2.35	–
FeNiCrCoBSiNb	12	30.43	3.57	0.05	12.04	–	39.60	2.88	9.88	–	1.55	–

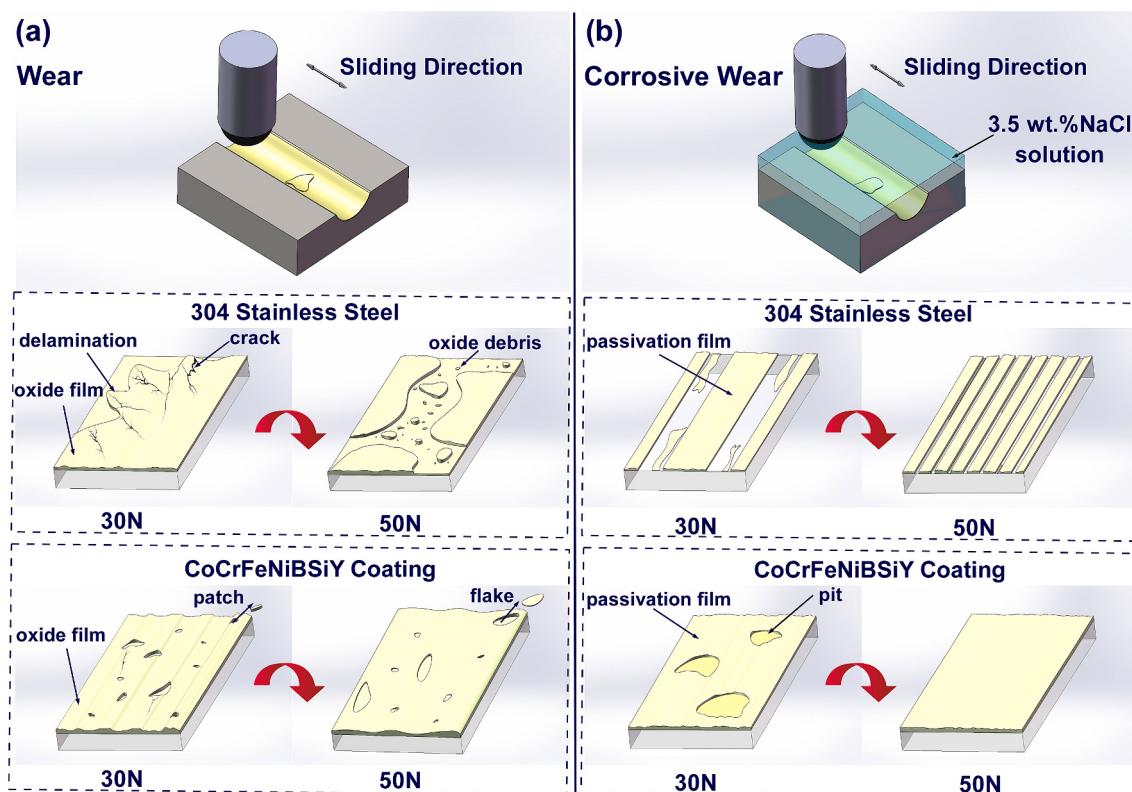


Fig. 13. The schematic diagram of dry wear and corrosive wear mechanisms of the CoCrFeNiBSiY coating and 304 stainless steel.

Fe/Cr in the oxide layer exceeds 3.4, indicating that the surface oxide layer contains a large amount of iron oxides. According to the Pilling-Bedworth ratio (P-B ratio) [52], if the RPB of the alloying element is <1 , the oxide layer is too thin, easily cracked, and has no protective effect (such as magnesium.). If $RPB > 2$, the oxide tends to flake off and provides no protection (e.g. iron.). If $1 < RPB < 2$, the oxide has a passivating effect (such as Al, Cr, Ni, Co, etc.). The RPB of Fe_2O_3 is 2.14. If the proportion of Fe element in the oxide layer formed on the coating surface is too high, the volume expansion caused by the oxidation process will be large, resulting in large internal stress inside the oxide layer. Therefore, the oxide layer is easily broken during friction and wear. This is also the main reason why the oxide layer on the surface of 304 stainless steel is broken when the load increases to 50 N. In addition, the Cr content in the oxide layer is low, and the bonding strength between the oxide layer and the coating is weak, which is not conducive to the formation of a dense and protective oxide layer. As reported by Bateni et al. [46], due to the lower hardness of 304 stainless steel, the wear mechanism under low loads is mainly the delamination of the surface layer. Adhesive wear was observed in dry wear tests with increasing load, consistent with the phenomenon reported in this study.

The microhardness of both CoCrFeNiBSiY and FeNiCrCoBSiNb coatings is approximately 3 times that of the 304 stainless steel. Fig. 10 shows that the wear rates of both coatings under 30 N conditions are about 1/3 of that of 304 stainless steel. It shows that the wear resistance of the materials is almost linearly inversely proportional to their hardness. Furthermore, the wear resistance of coatings with high hardness is less sensitive to load under dry friction conditions. Fig. 11 shows that under 30 N conditions, no cracks were found in the oxide layer formed on the surface of the CoCrFeNiBSiY coating. The oxide layer was mainly peeled off in the form of flakes. When the load increases to 50 N, the thickness of the oxide layer formed on the CoCrFeNiBSiY coating increases. The pit depth in the oxide layer is reduced. It can be inferred that increasing the load significantly accelerates the formation of a dense oxide layer. According to Tables 10 and 11, it can be found that

the Fe/(CoCrNi) ratio of the oxide layer formed on the surface of the CoCrFeNiBSiY coating does not exceed 0.4, which is much smaller than that of the FeNiCrCoBSiNb coating and 304 stainless steel. The high content of alloying elements results in good bonding strength between the oxide layer and the coating. This is the main reason why the CoCrFeNiBSiY coating exhibits excellent wear resistance properties.

4.3. Corrosive wear mechanism of laser cladded coatings and 304 stainless steel

The results show that there are great differences between the corrosive wear and dry wear behavior of both laser cladded coatings and 304 stainless steel. Normally, the volume loss rate of metal materials during corrosive wear should be higher than that under dry wear condition. The reason is that the passivation film generated on the material surface will be destroyed again due to wear. This will cause the passivation film on the coating surface to be in a passivation-destruction-repassivation cycle [53]. However, it is clearly found that the wear rate of both coatings under corrosive wear condition was significantly lower than that of dry wear, as shown in Fig. 10. This confirms that the passivation film generated on the surface of both coatings is not destroyed during the corrosive wear process. The schematic diagram of the corrosive wear mechanism is shown in Fig. 13(b).

The key factors that affect the corrosive wear resistance of metal materials are the passivation film, friction load, sliding speed, and the lubrication effect. According to Fig. 8, it can be inferred that the passivation current density of the CoCrFeNiBSiY coating is the smallest, while the passivation film formed on the surface of 304 stainless steel is denser. XPS analysis results found that the Cr/Fe ratio in the passivation film formed on the surface of the CoCrFeNiBSiY coating was 1.8, which was significantly higher than 0.15 of the FeNiCrCoBSiNb coating [27]. The results show that the corrosion resistance of CoCrFeNiBSiY coating is significantly superior to that of FeNiCrCoBSiNb coating. As shown in Figs. 11 and 12, the wear morphologies of both coatings and 304

stainless steel show typical furrows, indicating that the corrosive wear mechanism is mainly abrasive wear. Fu [18] et al. reported similar research results. It can be found that the passivation film formed on the surface of 304 stainless steel is partially removed during the corrosive wear process with a load of 30 N. When the load increased to 50 N, a similar phenomenon was also observed. In addition, the Fe/Cr ratio in the passive film remaining on the surface is high. These phenomena indicate that the bonding strength between the passivation film and 304 stainless steel substrate is weak. In addition, 304 stainless steel has poor repassivation ability in corrosive wear environments.

It was found that a dense passive film was formed on the surface of both coatings under all conditions in corrosive wear environments. The passivation film formed on the surface of the CoCrFeNiBSiY coating causes cracks in local areas due to wear under a load of 30 N. However, obvious repassivation occurred in the pits on the coating surface, as shown in Fig. 11(e). The difference is that the passivation film on the surface of FeNiCrCoBSiNb coating is partially removed, which is similar to the phenomenon on the surface of 304 stainless steel. When the friction load increases to 50 N, the passivation film formed on the surface of both coatings becomes relatively dense and uniform. The bonding strength between the passivation film and the coating is excellent. The volume wear rate of the CoCrFeNiBSiY coating is significantly lower than that of 304 stainless steel and FeNiCrCoBSiNb coating. Hua et al. [25] reported that the corrosion behavior of TiZrNbTaMo high-entropy alloy also significantly reduced the wear rate of the alloy in PBS solution. The EDS analysis results in Tables 10 and 11 show that the Fe/(CoCrNi) ratio of the passivation film on the surface of the CoCrFeNiBSiY coating increases from 0.3 to 0.6 as the friction load increases from 30 N to 50 N. However, the Fe/(CoCrNi) ratio of the passivation film on the FeNiCrCoBSiNb coating surface increased from 1.5 to 1.7. The smaller the Fe/(CoCrNi) ratio of the passivation film, the denser the passivation film and the better the bonding strength with the coating. The friction coefficient of the CoCrFeNiBSiY coating during corrosive wear process with a load of 50 N is the smallest (Fig. 9). It can be concluded that the CoCrFeNiBSiY coating has excellent corrosive wear resistance. In addition, the influence of lubrication on corrosive wear cannot be ignored. According to relevant research reports [25,26], corrosion solutions and corrosion products also play a lubricating role, thereby reducing the friction coefficient and inhibiting wear.

5. Conclusions

- (1) CoCrFeNiBSiY and FeNiCrCoBSiNb coatings were successfully prepared on 304 stainless steel substrate using laser cladding technology. Both coatings are mainly composed of FCC solid solution, boride, and Laves phases. The average microhardness of CoCrFeNiBSiY and FeNiCrCoBSiNb coatings are 578.6 HV_{0.2} and 632.5 HV_{0.2}, both of which are approximately 3 times that of 304 stainless steel.
- (2) The FeNiCrCoBSiNb coating has the lowest wear rate (0.0045 mm³/h) under dry wear condition with a load of 30 N. The dry wear resistance of both coatings and 304 stainless steel is almost linearly inversely proportional to their microhardness values. It is evident that the dry wear resistance of the FeNiCrCoBSiNb coating with high hardness is insensitive to changes in frictional load.
- (3) The CoCrFeNiBSiY coating exhibits superior corrosive wear resistance under different friction load conditions. This is mainly due to the excellent corrosion resistance of the coating as well as its repassivation capabilities. The passivation film on the surface of the CoCrFeNiBSiY coating becomes denser as the friction load increases.

CRediT authorship contribution statement

Zeng Junshan: Writing – original draft, Visualization, Validation,

Methodology, Investigation, Formal analysis, Data curation. **Chen Liang:** Visualization, Validation, Formal analysis, Data curation. **Lan Yuankuo:** Visualization, Methodology, Formal analysis, Data curation. **Cheng Yuhao:** Visualization, Validation, Investigation, Data curation. **Xu Luqian:** Visualization, Data curation. **Jiang Haoli:** Writing – review & editing, Methodology, Formal analysis, Conceptualization. **Ding Zhibing:** Writing – review & editing, Supervision, Investigation, Conceptualization. **Zhang Jianfeng:** Writing – review & editing, Supervision, Resources, Investigation, Conceptualization. **Liu Bin:** Writing – review & editing, Supervision, Resources, Investigation, Conceptualization. **Guo Wenmin:** Writing – review & editing, Writing – original draft, Supervision, Project administration, Investigation, Funding acquisition.

Declaration of competing interest

The authors declare that they have no known competing financial interests or personal relationships that could have appeared to influence the work reported in this paper.

Data availability

Data will be made available on request.

Acknowledgment

This research supported by the National Natural Science Foundation of China (52101208), the Hunan Provincial Natural Science Foundation (2022JJ50175), the Scientific Research Fund of Hunan Provincial Education Department (21A0465), and Graduate Innovation Project of Shaoyang University (CX2022SY019, CX2022SY021).

References

- [1] S. Eswarappa Prameela, T.M. Pollock, D. Raabe, M.A. Meyers, A. Aitkaliyeva, K.-L. Chintersingh, Z.C. Cordero, L. Graham-Brady, Materials for extreme environments, *Nat. Rev. Mater.* 8 (2022) 81–88, <https://doi.org/10.1038/s41578-022-00496-z>.
- [2] D. Cong-lin, B. Xiu-qin, Y. Xin-ping, Y. Cheng-qing, Research status and advances on tribological study of materials under ocean environment, *Tribology* 33 (2013) 311–320, <https://doi.org/10.16078/j.tribology.2013.03.014>.
- [3] E. Liu, Z. Zeng, W. Zhao, Corrosive wear and integrated anti-wear & anti-corrosion technology metallic materials in seawater, *Surf. Technol.* 46 (2017) 149–157, <https://doi.org/10.16490/j.cnki.issn.1001-3660.2017.11.021>.
- [4] Y. Zhang, X. Yin, J. Wang, F. Yan, Influence of microstructure evolution on tribocorrosion of 304SS in artificial seawater, *Corros. Sci.* 88 (2014) 423–433, <https://doi.org/10.1016/j.corsci.2014.07.062>.
- [5] J. Li, L. Pan, Q. Fu, Y. Zhou, N. Guo, Wettability and corrosion behavior of a Ni coating on 304 stainless steel surface, *Surf. Coat. Technol.* 357 (2019) 740–747, <https://doi.org/10.1016/j.surfcoat.2018.10.050>.
- [6] S. Mohan, S.S. Nair, A.V. Ajay, M.S. Senthil Saravanan, B.R. Vishnu, S. P. Sivapirakasam, M. Surianarayanan, Corrosion behaviour of ZrO₂-TiO₂ nano composite coating on stainless steel under simulated marine environment, *Mater. Today: Proc.* 27 (2020) 2492–2497, <https://doi.org/10.1016/j.mtpr.2019.09.224>.
- [7] Y. Zhang, T.T. Zuo, Z. Tang, M.C. Gao, K.A. Dahmen, P.K. Liaw, Z.P. Lu, Microstructures and properties of high-entropy alloys, *Prog. Mater. Sci.* 61 (2014) 1–93, <https://doi.org/10.1016/j.pmatsci.2013.10.001>.
- [8] Y. Li, K. Wang, H. Fu, X. Guo, J. Lin, Microstructure and wear resistance of in-situ TiC reinforced AlCoCrFeNi-based coatings by laser cladding, *Appl. Surf. Sci.* 585 (2022) 152703, <https://doi.org/10.1016/j.apsusc.2022.152703>.
- [9] D. Kumar, Recent advances in tribology of high entropy alloys: a critical review, *Prog. Mater. Sci.* 136 (2023) 101106, <https://doi.org/10.1016/j.pmatsci.2023.101106>.
- [10] Y. Li, H. Fu, K. Wang, X. Yang, B. Zong, J. Lin, Effect of Mo addition on microstructure and wear resistance of laser clad AlCoCrFeNi-TiC composite coatings, *Appl. Surf. Sci.* 623 (2023) 157071, <https://doi.org/10.1016/j.apsusc.2023.157071>.
- [11] X. Hao, H. Liu, X. Zhang, J. Tao, Y. Wang, C. Yang, Y. Liu, Microstructure and wear resistance of in-situ TiN/(Nb, Ti)Si₃ reinforced MoNbTaWTi-based refractory high entropy alloy composite coatings by laser cladding, *Appl. Surf. Sci.* 626 (2023) 157240, <https://doi.org/10.1016/j.apsusc.2023.157240>.
- [12] W. Yuan, R. Li, Z. Chen, J. Gu, Y. Tian, A comparative study on microstructure and properties of traditional laser cladding and high-speed laser cladding of Ni45 alloy coatings, *Surf. Coat. Technol.* 405 (2021) 126582, <https://doi.org/10.1016/j.surfcoat.2020.126582>.

- [13] L. Zhu, P. Xue, Q. Lan, G. Meng, Y. Ren, Z. Yang, P. Xu, Z. Liu, Recent research and development status of laser cladding: a review, *Opt. Laser Technol.* 138 (2021) 106915, <https://doi.org/10.1016/j.optlastec.2021.106915>.
- [14] C. Liu, X. Qiu, J. Peng, Z. Wang, Structure and properties of laser cladding CoCrNi multicomponent alloy coating used in rain gauge, *Opt. Lasers Eng.* 163 (2023) 107458, <https://doi.org/10.1016/j.optlaseng.2022.107458>.
- [15] G. Ma, H. Cui, D. Jiang, H. Chen, X. Hu, G. Zhang, R. Wang, X. Sun, X. Song, The evolution of multi and hierarchical carbides and their collaborative wear-resisting effects in CoCrNi/WC composite coatings via laser cladding, *Mater. Today Commun.* 30 (2022) 103223, <https://doi.org/10.1016/j.mtcomm.2022.103223>.
- [16] C. Suryanarayana, A. Inoue, *Bulk Metallic Glasses*, CRC Press, 2017.
- [17] R.L. Li, J. Li, Y.N. Yan, M. Shao, J. Li, Tribocorrosion resistance of CoCrFeNiNb laser-clad coatings in the neutral and acid solutions, *Opt. Laser Technol.* 158 (2023) 108817, <https://doi.org/10.1016/j.optlastec.2022.108817>.
- [18] Y. Fu, C. Huang, C. Du, J. Li, C. Dai, H. Luo, Z. Liu, X. Li, Evolution in microstructure, wear, corrosion, and tribocorrosion behavior of Mo-containing high-entropy alloy coatings fabricated by laser cladding, *Corros. Sci.* 191 (2021) 109727, <https://doi.org/10.1016/j.corsci.2021.109727>.
- [19] Y. Zhang, J. Guo, G. Xu, Z. Li, S. Wei, et al., *Appl. Surf. Sci.* 611 (2023) 155587, <https://doi.org/10.1016/j.apsusc.2022.155587>.
- [20] S.S. Joshi, S. Katakanam, H. Singh Arora, S. Mukherjee, N.B. Dahotre, Amorphous coatings and surfaces on structural materials, *Crit. Rev. Solid State Mater. Sci.* 41 (2015) 1–46, <https://doi.org/10.1080/10408436.2015.1053602>.
- [21] X. Shang, C. Zhang, T. Xv, C. Wang, K. Lu, Synergistic effect of carbide and amorphous phase on mechanical property and corrosion resistance of laser-clad Fe-based amorphous coatings, *Mater. Chem. Phys.* 263 (2021) 124407, <https://doi.org/10.1016/j.matchemphys.2021.124407>.
- [22] H. Zhang, H. Cui, C. Man, F. Liu, K. Pang, G. Ma, H. Chen, Z. Cui, The tribocorrosion resistance of TiN+TiB /TC4 composite coatings and the synergistic strengthening effects of multi-level reinforcements, *Corros. Sci.* 219 (2023) 111224, <https://doi.org/10.1016/j.corsci.2023.111224>.
- [23] J. Feng, H. Xiao, Tribocorrosion behavior of laser cladded Ti-Al-(C, N) composite coatings in artificial seawater, *Coatings* 12 (2022) 187, <https://doi.org/10.3390/coatings1220187>.
- [24] X. Wen, X. Cui, G. Jin, Y. Liu, Y. Zhang, X. Zhang, E. Liu, H. Tian, Y. Fang, Corrosion and tribo-corrosion behaviors of nano-lamellar Ni_{1.5}CrCoFe0.5Mo0.1Nb_x eutectic high-entropy alloy coatings: the role of dual-phase microstructure, *Corros. Sci.* 201 (2022) 110305, <https://doi.org/10.1016/j.corsci.2022.110305>.
- [25] N. Hua, W. Wang, Q. Wang, Y. Ye, S. Lin, L. Zhang, Q. Guo, J. Brechtl, P.K. Liaw, Mechanical, corrosion, and wear properties of biomedical Ti-Zr-Nb-Ta-Mo high entropy alloys, *J. Alloys Compd.* 861 (2021) 157997, <https://doi.org/10.1016/j.jallcom.2020.157997>.
- [26] C. Cao, Y. Wang, C. Zhang, D. Niu, Y. Si, J. Si, Z. Shi, Y. He, Tribocorrosion behavior of laser cladding FeCrNiCoMoCuBSi high entropy alloy coating, *Rare Metal Mater. Eng.* 52 (2023) 1439–1446, <https://doi.org/10.12442/j.issn.1002-185X.20220227>.
- [27] H. Zhang, W. Li, H. Xu, L. Chen, J. Zeng, Z. Ding, W. Guo, B. Liu, Microstructure and corrosion behavior of laser cladding FeCoNiCrBSi based high-entropy alloy coatings, *Coatings* 12 (2022) 628, <https://doi.org/10.3390/coatings12050628>.
- [28] K. Chong, Y. Gao, Z. Zhang, Y. Zou, X. Liang, Thermal stability and corrosion behavior of a novel Zr22.5Ti22.5Hf22.5Ni22.5Ta10 high-entropy amorphous alloy, *Corros. Sci.* 213 (2023) 110979, <https://doi.org/10.1016/j.corsci.2023.110979>.
- [29] J.Y. Aguilar-Hurtado, A. Vargas-Uscategui, L.G. Torres-Mejia, L. Mujica-Ronceny, D. Zambrano-Mera, S. Pantaleone, B. Wang, A. Rosenkranz, K. Paredes-Gil, Experimental and computational analysis of stacking fault energy in B-doped Fe50–XMn30Co10Cr10BX multi-principal elements alloys, *J. Alloys Compd.* 969 (2023) 172428, <https://doi.org/10.1016/j.jallcom.2023.172428>.
- [30] H.-z. Wang, Y.-h. Cheng, X.-c. Zhang, J.-y. Yang, C.-m. Cao, Effect of laser scanning speed on microstructure and properties of Fe based amorphous/nanocrystalline cladding coatings, *Mater. Chem. Phys.* 250 (2020), <https://doi.org/10.1016/j.matchemphys.2020.123091>.
- [31] G. Huang, L. Qu, Y. Lu, Y. Wang, H. Li, Z. Qin, X. Lu, Corrosion resistance improvement of 45 steel by Fe-based amorphous coating, *Vacuum* 153 (2018) 39–42, <https://doi.org/10.1016/j.vacuum.2018.03.042>.
- [32] Z. Ma, C. Xia, H. Zhong, T. Yang, N. Liu, C. Liang, Q. Li, Microstructure, mechanical property and corrosion resistance of FeCoCrNi-M high-entropy alloy coatings on 6061 aluminum alloy prepared by laser cladding, *Surf. Coat. Technol.* 455 (2023) 129217, <https://doi.org/10.1016/j.surfcoat.2022.129217>.
- [33] H. Zhang, Y. Pan, Y.-Z. He, Synthesis and characterization of FeCoNiCrCu high-entropy alloy coating by laser cladding, *Mater. Des.* 32 (2011) 1910–1915, <https://doi.org/10.1016/j.matdes.2010.12.001>.
- [34] C. Zhang, G.J. Chen, P.Q. Dai, Evolution of the microstructure and properties of laser-clad FeCrNiCoB high-entropy alloy coatings, *Mater. Sci. Technol.* 32 (2016) 1666–1672, <https://doi.org/10.1080/02670836.2015.1138035>.
- [35] X. Wen, X. Cui, G. Jin, Y. Liu, Y. Zhang, Y. Fang, In-situ synthesis of nano-lamellar Ni1.5CrCoFe0.5Mo0.1Nb_x eutectic high-entropy alloy coatings by laser cladding: alloy design and microstructure evolution, *Surf. Coat. Technol.* 405 (2021) 126728, <https://doi.org/10.1016/j.surfcoat.2020.126728>.
- [36] T. Zhang, H. Liu, J. Hao, P. Chen, H. Yang, Evaluation of microhardness, tribological properties, and corrosion resistance of CrFeNiNbTi high-entropy alloy coating deposited by laser cladding, *J. Mater. Eng. Perform.* 30 (2021) 9245–9255, <https://doi.org/10.1007/s11665-021-06107-2>.
- [37] J. Cheng, B. Sun, Y. Ge, X. Hu, L. Zhang, X. Liang, X. Zhang, Nb doping in laser-clad Fe25Co25Ni25(B0.7Si0.3)25 high entropy alloy coatings: microstructure evolution and wear behavior, *Surf. Coat. Technol.* 402 (2020) 126321, <https://doi.org/10.1016/j.surfcoat.2020.126321>.
- [38] M. Wang, Y. Lu, G. Zhang, H. Cui, D. Xu, N. Wei, T. Li, A novel high-entropy alloy composite coating with core-shell structures prepared by plasma cladding, *Vacuum* 184 (2021) 109905, <https://doi.org/10.1016/j.vacuum.2020.109905>.
- [39] Z. Zhou, B. Liu, W. Guo, A. Fu, H. Duan, W. Li, Corrosion behavior and mechanism of FeCrNi medium entropy alloy prepared by powder metallurgy, *J. Alloys Compd.* 867 (2021) 159094, <https://doi.org/10.1016/j.jallcom.2021.159094>.
- [40] E. Hao, X. Liu, Y. An, H. Zhou, F. Yan, The coupling effect of immersion corrosion and cavitation erosion of NiCoCrAlYTa coatings in artificial seawater, *Corros. Sci.* 169 (2020) 108635, <https://doi.org/10.1016/j.corsci.2020.108635>.
- [41] K. Feng, Y. Zhang, Z. Li, C. Yao, L. Yao, C. Fan, Corrosion properties of laser cladded CrCoNi medium entropy alloy coating, *Surf. Coat. Technol.* 397 (2020) 126004, <https://doi.org/10.1016/j.surfcoat.2020.126004>.
- [42] G. Antou, G. Montavon, F. Hlawka, A. Cornet, C. Coddet, Exploring thermal spray gray alumina coating pore network architecture by combining stereological protocols and impedance electrochemical spectroscopy, *J. Therm. Spray Technol.* 15 (2006) 765–772, <https://doi.org/10.1361/105996306X147045>.
- [43] X. Gong, Y. Cui, D. Wei, B. Liu, R. Liu, Y. Nie, Y. Li, Building direction dependence of corrosion resistance property of Ti-6Al-4V alloy fabricated by electron beam melting, *Corros. Sci.* 127 (2017) 101–109, <https://doi.org/10.1016/j.corsci.2017.08.008>.
- [44] X. Li, J. Liang, T. Shi, D. Yang, X. Chen, C. Zhang, Z. Liu, D. Liu, Q. Zhang, Tribological behaviors of vacuum hot-pressed ceramic composites with enhanced cyclic oxidation and corrosion resistance, *Ceram. Int.* 46 (2020) 12911–12920, <https://doi.org/10.1016/j.ceramint.2020.02.057>.
- [45] R. Shah, N. Pai, A. Rosenkranz, K. Shirvani, M. Marian, Tribological behavior of additively manufactured metal components, *J. Manuf. Mater. Process.* 6 (2022) 138, <https://doi.org/10.3390/jmmp6060138>.
- [46] M.R. Bateni, J.A. Szpunar, X. Wang, D.Y. Li, Wear and corrosion wear of medium carbon steel and 304 stainless steel, *Wear* 260 (2006) 116–122, <https://doi.org/10.1016/j.wear.2004.12.037>.
- [47] X. Ji, C. Luo, J. Jin, Y. Zhang, Y. Sun, L. Fu, Tribocorrosion performance of 316L stainless steel enhanced by laser clad 2-layer coating using Fe-based amorphous powder, *J. Mater. Res. Technol.* 17 (2022) 612–621, <https://doi.org/10.1016/j.jmrt.2022.01.046>.
- [48] H. Chen, H. Cui, D. Jiang, X. Song, L. Zhang, G. Ma, X. Gao, H. Niu, X. Zhao, J. Li, C. Zhang, R. Wang, X. Sun, Formation and beneficial effects of the amorphous/nanocrystalline phase in laser remelted (FeCoCrNi)75Nb10BSi7 high-entropy alloy coatings fabricated by plasma cladding, *J. Alloys Compd.* 899 (2022) 163277, <https://doi.org/10.1016/j.jallcom.2021.163277>.
- [49] X. Yang, Y. Zhang, Prediction of high-entropy stabilized solid-solution in multi-component alloys, *Mater. Chem. Phys.* 132 (2012) 233–238, <https://doi.org/10.1016/j.matchemphys.2011.11.021>.
- [50] M. Ma, A. Han, Z. Zhang, Y. Lian, C. Zhao, J. Zhang, The role of Si on microstructure and high-temperature oxidation of CoCr2FeNb0.5Ni high-entropy alloy coating, *Corros. Sci.* 185 (2021) 109417, <https://doi.org/10.1016/j.corsci.2021.109417>.
- [51] J. Archard, Contact and rubbing of flat surfaces, *J. Appl. Phys.* 24 (1953) 981–988, <https://doi.org/10.1063/1.1721448>.
- [52] N. Pilling, The oxidation of metals at high temperature, *J. Inst. Met.* 29 (1923) 529–582.
- [53] Z. Li, H. Yu, D. Sun, The tribocorrosion mechanism of aluminum alloy 7075-T6 in the deep ocean, *Corros. Sci.* 183 (2021) 109306, <https://doi.org/10.1016/j.corsci.2021.109306>.